Accuracy Improvement and Joint Stiction Relieve in Robot Arms Movement Applying Torque-Based Cartesian Impedance Control With Dithering

Salvador Monzó Martínez
Altin Zejnullahu

LUND
UNIVERSITY

Department of Automatic Control

MSc Thesis TFRT-6202
ISSN 0280–5316

Department of Automatic Control
Lund University
Box 118
SE-221 00 LUND
Sweden

Printed in Sweden by Media-Tryck.
Lund 2023

Abstract

Robots are nowadays present and essential in a wide range of applications, and robot arms in particular are capable of performing various tasks such as inspection, material handling, and welding. They can be classified into several types, depending on their structure and purpose. This project focuses on two collaborative robot arms, a type that is designed to work in the presence of human interaction. They both possess a manipulator at the end of the arm known as end effector, which normally realizes the tasks and is responsible for following trajectories instructed by the controller.

One of the challenges faced by robot arms is static friction in the joints, also known as stiction. This phenomenon generally occurs in low-speed regimes, having its main component expected at zero velocity, and might affect the robot's motion and therefore its accuracy. During this thesis work, stiction will be characterized through different approaches and its impact will be mitigated by applying a technique known as dithering. Dithering consists of adding a periodic signal, in this case a sinusoidal wave, to the robot controller in order to reduce the stiction effect. A particular dithering signal can be built for each of the robot joints since their dynamics are also different between them.

Two approaches were designed to characterize the stiction. The first approach involves the identification of the robot dynamics, while the second approach, referred to as the Single Joint Experiment (SJE), is an empirical iterative method in which the robot arm conducts individualized motions for each joint.

Subsequently, dithering signals were built after characterizing the stiction bands, and applied to different motion experiments. The SJE was first improved by reducing the minimum torque needed to surpass stiction, and at the same time this procedure was used to obtain the optimal parameters for the joints' dithering signals. Finally, applying these optimal dithering signals to the controller, the deviations in the trajectories were also reduced, resulting in improved accuracy.

Keywords: robot arm, collaborative robot, joint, dithering, static friction, stiction, Cartesian impedance control

Acknowledgements

We would like to thank our supervisor Ph.D. student Matthias Mayr, for the idea and introduction into this project, the incessant help provided during the hours and hours of experiments with the LBR iiwa arm, and the continuous supervision and advice.

We would also like to thank our other supervisor Ph.D. student Julian M. Salt-Ducaju for his continuous support and guidance during this thesis. He was of tremendous help with the experiments done and learning issues with the Panda arm, with understanding all the theory background needed for preparing this work and the supervision role realized during all this time.

We are also very thankful to our examiner Dr. Björn Olofsson for bringing us the opportunity of working in this thesis project, helping us with every general inconvenience and providing brilliant ideas to the experiments design.

Finally, we are very grateful to our families for their unconditional support and love. Does not matter when and where, they have always been there for us.

Contents

1

Introduction

Robots are, without a doubt, an essential tool around the world nowadays. Not only do they provide uncountable working conveniences in every field related to engineering, but also help the technology itself to evolve. They can achieve high levels of accuracy, productivity, flexibility, safety and efficiency; with or without human interaction.

Among all kinds of robots, robot arms are known to be present in a huge number of applications: from manipulation to inspection, and even in specific tasks such as medical surgeries. Robot arms are made up of different links that are connected by joints, which are actuated by different motors. The end of the arm is commonly known as end effector, and it is the part that normally realizes the tasks and follows the trajectories that are sent to the robot by the controller [Lee, 1982].

Robot arms can be classified into several types depending on their form and uses: articulated, Cartesian, cylindrical, delta, polar/spherical, and Selective Compliance Articulated Robot Arm (abbreviated as SCARA) [Siciliano and Khatib, 2007]. These also include subcategories such as collaborative robot arms. Collaborative robot arms are meant to work in the presence of human interaction by providing sensors and safety measures that prevent hazardous situations toward people working together with them. [*6 Types of Industrial Robotic Arms* 2023]. This thesis work will focus on two collaborative robot arms that can be seen in Figure 1.1.

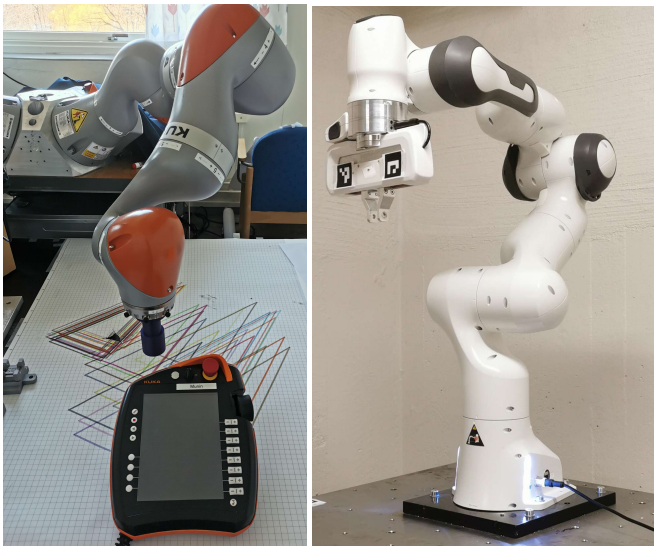

Figure 1.1 LBR iiwa by KUKA AG (left) and Franka Emika Robot, also known as Panda Arm, by Franka Emika (right).

The joints of a robot arm might suffer from stiction (*i.e.*, static friction) when, for example, performing a short movement from an initial or static position. Static friction is a component of friction that can come from the interlocking of surface irregularities, material deformations, the stickiness of the surfaces contact, or even because of the surface roughness or abrasion [*6 Major Causes Of Static Friction* 2023]. This phenomenon occurs for near-zero velocities, having its main component expected at zero velocity, and might induce error in the end-effector trajectory, which can be problematic since a lack of precision could produce failures in tasks that require high accuracy levels.

Different techniques can be applied to minimize the stiction problem. Dithering is one of them, which consists of an induced oscillatory signal that is applied directly to the commanded torques sent to the robot joints with the aim of overcoming the stiction [Stolt et al., 2015]. The dithering signals that will be used in this project are sinusoidal, with an amplitude and frequency that will be designed individually for each of the robot arm joints. In order to determine these variables, stiction will be characterized first.

1.1 Problem Statement

The main objective of this thesis is to find and compensate for the static friction that naturally exists within the joints of the robot arm to reduce the error on the real system and to increase the motion's accuracy. Since robots are often simulated without any friction modeled in the articulations, a gap between reality and simulation is created.

In order to achieve this objective, it is first necessary to identify and model the stiction in each of the joints. A control strategy is designed based on torque-driven experiments that use a *Cartesian Impedance Controller* [Mayr and Salt-Ducaju, 2022], realized through the open-source package collection known as Robot Operating System (ROS) to run the real robot arms [Quigley et al., 2009]. This strategy, which will be explained step by step in Chapter 3, was applied on two real 7-DoF (degrees of freedom) state-of-the-art robot arms: LBR iiwa [*LBR iiwa KUKA Datasheet* 2023] by KUKA AG and Franka Emika Robot [*Franka Emika Robot's Datasheet* 2023], also known as Panda Arm, by Franka Emika (see Figure 1.1).

Related Work

This project shares similarities with previous work such as [Holmesson, 2021], [Chouman, 2021], and [Stolt, 2015]. Articles such as [Salt Ducaju et al., 2021] and [Dong et al., 2012] were also reviewed.

In the first thesis work, Joel Holmesson applied admittance control with a position controller and he worked on bringing the Cartesian controller's package to the LBR iiwa robot arm setup [Holmesson, 2021], which will be used in this project. In the second related work, Oussama Chouman's objective was developing and evaluating a control strategy using ROS and Cartesian impedance control for the LBR iiwa arm as well [Chouman, 2021]. This simulation experimental procedure from Oussama Chouman is included in this thesis experiments. The work by Andreas Stolt used a different robot arm and applied direct force control, which is a distinct control strategy [Stolt, 2015]. However, it provides very interesting and helpful information since dithering was implemented to increase the accuracy of force estimation. Among other articles, Julian M. Salt-Ducaju's work was reviewed in order to learn about nullspace motion [Salt Ducaju et al., 2021]. Additionally, Xiao Xing Dong's article was studied for having another example of Cartesian impedance control implementation [Dong et al., 2012].

Scientific Basis. In this project, the impedance control in Cartesian space follows the theory written in the book by Ott [Ott, 2008], in which he described the principles and application of torque-based Cartesian impedance control. The friction model used for the joint motors includes the Stribeck effect [Corke, 2017].

1.2 Aim and Limitations

This project develops a strategy for parameterizing the static friction found in robot arms joints as well as for reducing the effects of it when reproducing specified trajectories with Cartesian impedance control. In this case, this process has been applied to collaborative robot arms, but could be extrapolated to other types of robot arms, since the approach follows the theoretical principles that all robot arms share. The results obtained should lead to more accurate trajectories and therefore to a safer and more efficient environment for robot arms. Furthermore, it might also help future projects that will recreate similar processes and pipelines based on the same theoretical foundation and principles that were already existent. In summary, the procedure developed during this thesis will prevail as a skeleton of how to handle the stiction problem using the control strategy considered here.

As a limitation, it could be said that this thesis follows an approach that chooses a specific way to characterize stiction, as well as how to mitigate its impact. Other approaches, such as using a higher-order friction model or a different estimation method, could be more precise when modeling the behavior of the robot joints. The dithering technique has its own limitations and drawbacks, producing vibrations in the robot. Some equipment issues, such as calibration problems in the LBR iiwa, were also found and will be discussed later on this paper.

1.3 Outline

The structure of the report is shaped as follows:

2 — Background
Presents the necessary theoretical basis for robotics and control such as kinematics and dynamics, as well as some key concepts from physics regarding friction.

3 — Implementation
Describes the robot setup, software interfaces, and methodology used in the project. This includes how the *Cartesian Impedance Controller* has been implemented and the steps followed in order to achieve the desired results.

4 — Results
Explains the concept behind the experiments and presents the results.

5 — Discussion
Interprets the results and argues the validity of the applied method. The objective of the thesis is compared with the results and suggested ideas for future work are presented.

6 — Conclusions
The summary of the thesis, with emphasis on the project objective, main contributions, and results.

1.4 Individual Contributions

Both authors made significant contributions to the project, with distinct responsibilities in both the practical and written aspects.

In the practical implementation of the project, Altin took the lead in writing the necessary code, while Salvador played a crucial role in ensuring that safety measures were in place to prevent accidents. The authors collaborated closely, actively participating in discussions, brainstorming ideas, and finding solutions to various challenges encountered during the project.

For the written part, the workload was divided among us, with each member taking responsibility for specific sections. Salvador took the lead in writing the *Introduction* chapter. In the *Background* chapter, Salvador focused on the topics: *Cartesian Impedance Control*, *Control Design*, *Friction*, and *Dithering*. In the *Implementation* chapter, Salvador took charge of the *LBR iiwa setup* and the *Approach and Methodology*. Altin covered topics such as the *Basics of Robotics*, *Kinematics*, *Dynamics* in the *Background* chapter, and *Panda Arm* and *Software* in the *Implementation* chapter.

The authors worked together on the *Results* chapter, both in the writing part and in the creation of figures and tables. Additionally, the authors shared the responsibility of writing the *Discussion* and *Conclusion* chapters, where we combined our perspectives and insights.

Overall, the authors complemented each other's expertise, shared ideas, and provided valuable contributions throughout the project, both in practical implementation and written documentation.

2

Background

This chapter introduces the theoretical foundations necessary to understand the contents of the project. Concepts are mainly based on physics, automation, and control.

2.1 Basics of Robotics

Robots can generally be classified as either robot manipulators or mobile robots [Siciliano et al., 2008]. Robot manipulators have their base fixed, while mobile robots, as their name suggests, have a mobile base. There are also hybrids with a mobile base and a manipulator mounted on them. Robot manipulators will be the focus of this thesis.

Robot Manipulators

Robot manipulators are robotic arms designed to manipulate and interact with their environment. The most common among robot manipulators is the serial link manipulator [Corke, 2017].

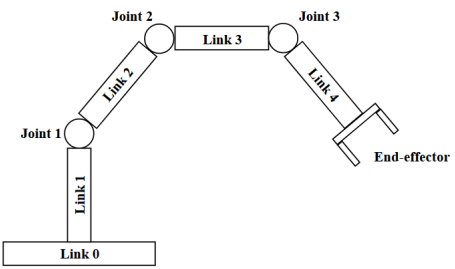

Figure 2.1 A simple serial link manipulator with three joints and a gripper end effector.

The structure usually consists of multiple interconnected segments, called links, which are connected by joints. The joints, in turn, allow the links to move relative

to each other. At the end of this chain of links and joints is the end effector that is used to manipulate the objects in its environment. The type of end effector can vary from grippers to welding torches, depending on the task.

There are several types of joints used in robotics, such as prismatic, revolute, or spherical joints. Prismatic joints allow translation along a single axis, whilst revolute joints allow rotation along a single axis. Spherical joints provide more complex movements since they allow rotation in three perpendicular axes. In robotic arms revolute joints are usually preferred due to their compactness and reliability [Siciliano et al., 2008]. Each revolute joint provides the manipulator with a single degree of freedom.

The set of all possible joint configurations is often referred to as the joint space and it contains all possible combinations of joint angles that can be achieved by the manipulator. The workspace refers to the set of all possible positions and orientations that the end effector can reach. It is the space in which the robot can interact with the environment.

The number of degrees of freedom required to perform a task in a 3D space depends on the complexity of the task and the constraints involved. In general, a minimum of six degrees of freedom is required to fully control the position and orientation of an object in a 3D space [Siciliano et al., 2008]. These six degrees of freedom are often represented by the x, y, and z translation axes and the pitch, roll, and yaw rotation axes. If more degrees of freedom than required are available in the robot it is said that the manipulator is redundant from a kinematic viewpoint. Then, there are an infinite number of ways to configure the links while still having the same end-effector pose. This allows for more complex movements, such as avoiding obstacles or maintaining a specific orientation of the end effector while moving in a constrained environment. A movement of the arm where the position and orientation of the end effector is not affected is called nullspace motion [Siciliano et al., 2008]. The nullspace refers to the subspace of the joint space in which the end-effector pose is not affected. In other words, it is the set of joint configurations that result in the same end-effector pose.

2.2 Kinematics

In robotics, kinematics refers to the study of the motion of the robot without considering the forces that cause the motion [Craig, 1989]. It describes the relationship between the joint positions and the end-effector position and orientation. When manipulating an object in the workspace, it is necessary to describe the position and orientation (pose) of the end effector. The end effector is typically at one end of the chain of links whilst the base is at the other end. The resulting motion of the manipulator is made up of the motions of each link. Computing the end-effector pose from the joint positions is called forward kinematics and computing the joint positions from the end-effector pose is called inverse kinematics [Craig, 1989].

Forward Kinematics

The mapping from joint variables to the end-effector pose is known as forward kinematics. Forward kinematics is commonly performed using a series of homogeneous transformation matrices that relate the pose at each joint to the pose at the previous joint in the manipulator kinematic chain [Spong and Vidyasagar, 1989].

These transformation matrices are not constant as they are functions of a single joint variable (joint angle). These matrices are then applied in sequence from the base link to the end effector to obtain the transformation matrix for the entire robot, which can be used to obtain the pose of the end effector in the base coordinate system. However, this computation can become complex with an n-link manipulator, especially as n grows, and conventions such as the Denavit-Hartenberg (DH) convention [Spong and Vidyasagar, 1989] are introduced to simplify the analysis. The DH convention provides a systematic way to assign frames to each joint and, by doing so, reduces the number of variables required to describe the position and orientation of robots from six to four [Spong and Vidyasagar, 1989]. This reduces the complexity considerably and makes kinematic analysis more manageable and allows for easier control and trajectory planning.

Jacobian

The two previous sections dealt with the relationship between joint configurations and the end-effector pose. The Jacobian is a matrix of partial derivatives which relates the rate of change of the end-effector's pose to the rate of change of the joint angles [Craig, 1989]. The Jacobian can be used to calculate the linear and angular velocities of the end effector, given the velocities of the manipulator's joints. The Jacobian matrix can be calculated through two approaches: analytical and geometric. The analytical Jacobian is derived directly from the forward kinematics whereas the computation of the geometric Jacobian uses a geometric technique.

Geometric Jacobians can have numerically unstable inverses when the manipulator is close to a singularity, which is a configuration in which one or more degrees of freedom are lost [Craig, 1989]. Singularities can be categorized into two types: boundary and internal. Boundary singularities occur when the joints are at their limit either by being outstretched or fully retracted. These types of singularities are not that serious since they can be avoided. Internal singularities are caused by lining up two or more joint axes. Internal singularities are a serious problem since they can occur anywhere in the workspace. Singularities are a problem because they may cause the manipulator to be unable to move in certain directions or achieve certain positions.

2.3 Dynamics

As kinematics refer to the study of the motion of a robot without considering the forces that cause the motion, dynamics refers to the study of the relationship between the motion of a robot and the forces and torques acting on it [Spong and Vidyasagar, 1989]. It is a crucial part for both the simulation and control of robotic systems, as they can be used to predict the behavior of a robot under different conditions.

In robotics, a rigid body is a body that does not deform and can be modeled as a set of points that have a fixed distance from each other regardless of the force exerted on it. On the other hand, a non-rigid body is deformable, meaning it changes its shape under applied forces. Rigid-body assumptions simplify the modeling and control of the robot, since they do not take into account deformations. To be able to apply these simplifications, from now on, the robot will be assumed to be a rigid-body manipulator.

There are two types of problems to solve [Craig, 1989]. The first problem is finding the required vector of joint torques, τ, given a trajectory point (joint position q, joint velocity $\dot{q}$, and joint acceleration $\ddot{q}$) known as the inverse dynamics problem. The other problem, known as the forward dynamics problem, is to calculate the resulting motion of the manipulator $q, \dot{q}, \ddot{q}$, given the torque vector τ.

There are multiple approaches on deriving the equations of motion for a rigid-body manipulator. One of them is the Lagrange formulation. In the Lagrange formulation, the dynamics of the robotic system are described based on the Lagrangian, which is the difference between the kinetic and potential energies of the system [Siciliano et al., 2008]

$$L = T - U \tag{2.1}$$

where T is the total kinetic energy of the system and U is the total potential energy. The kinetic energy is a function of the velocities of the joints, while the potential energy is a function of the position of the joints.

$$L(q,\dot{q}) = T(q,\dot{q}) - U(q) \tag{2.2}$$

Rewriting Newton's second law in terms of the Lagrangian, known as the Euler-Lagrange equation

$$\frac{d}{dt}\left(\frac{\partial}{\partial \dot{q}}L\right) - \frac{\partial}{\partial \dot{q}}L = \tau \tag{2.3}$$

and applying them to an n-link rigid-body manipulator we obtain the following equation [Spong and Vidyasagar, 1989]

$$M(q)\ddot{q} + C(q,\dot{q})\dot{q} + g(q) = \tau - \tau_f \tag{2.4}$$

where $M(q) \in \mathbb{R}^{n\times n}$ is the inertia matrix, $C(q,\dot{q}) \in \mathbb{R}^{n\times n}$ is the Coriolis/centrifugal matrix, $g(q) \in \mathbb{R}^n$ are the gravitational terms, τ the joint torques and τ_f the friction torques. This equation can be used for the inverse dynamics problem, *i.e.*, given $q, \dot{q}, \ddot{q}$ compute the joint torques.

The solution to the forward dynamics problem can be obtained by isolating q from the equation of the inverse dynamics problem

$$\ddot{q} = M(q)^{-1}(\tau - \tau_f - C(q,\dot{q})\dot{q} - g(q)) \tag{2.5}$$

and $q, \dot{q}$ can subsequently be obtained by integrating $\ddot{q}$ solving the forward dynamics problem. If free-space motion cannot be guaranteed because of the environment dynamics, the external torques applied from the robot to the environment τ_{ext} can be added to the Equation (2.4) and results in

$$\tau - \tau_f - [M(q)\ddot{q} + C(q,\dot{q})\dot{q} + g(q)] = \tau_{ext} \tag{2.6}$$

2.4 Cartesian Impedance Control

Impedance control is a control strategy used in robotics and mechatronics to regulate the interaction between a robot and its environment [Chouman, 2021]. It consists of a virtual mass-spring-damper system concept applied to, in this case, a manipulator. The idea is to assume the robot as an impedance while the environment as an admittance so that a dynamic relationship between the external torques and the robot motion can be established [Ott, 2008].

This concept was introduced by Hogan, supposing that it was impossible to devise a controller that would cause a physical system to display an apparent behavior to its environment that is distinguishable from that of a purely physical system [Hogan, 1984]. Following this hypothesis, he formulated the model of the target impedance dynamics, which is based on the target inertia M_d, target damping D_d and the target stiffness K_d. Impedance control provides a compliant robot motion simply by monitoring the dynamic behavior of the manipulator.

When impedance control is formulated in Cartesian space, Cartesian impedance control is obtained. Transforming Equation (2.6) into Cartesian space the resulting equation is

$$M_x(x)\ddot{x} + C_x(x,\dot{x})\dot{x} + g_x(x) = F - F_f - F_{ext} \tag{2.7}$$

where $M_x(x) \in \mathbb{R}^{n\times n}$ is the Cartesian inertia matrix, $C_x(x,\dot{x}) \in \mathbb{R}^{n\times n}$ is the Cartesian Coriolis matrix, $g_x(x) \in \mathbb{R}^n$ is the Cartesian gravity term, F are the joint forces, F_f are the friction forces and F_{ext} are the external forces [Ott, 2008]. It is important to mention that the friction forces F_f and torques τ_f are usually removed from the control law's theory since they bring many nonlinearities with them. However, they are the main focus of this project and will be taken into account when the control laws are applied to the real system so the friction torques τ_f can be calculated.

The geometrical Jacobian J is the tool that allows projection of all these matrices and variables in Cartesian space as follows

$$\begin{aligned} M_x(x) &= J^{-T}(q)M(q)J^{-1}(q) \\ C_x(x,\dot{x}) &= J^{-T}(q)[C(q,\dot{q}) - M(q)J^{-1}(q)\dot{J}(q)]J^{-1}(q) \\ g_x(x) &= J^{-T}(q)g(q) \\ F &= J^{-T}(q)\tau \end{aligned} \tag{2.8}$$

As observed in Equation (2.8), the inverse geometrical Jacobian J^{-1} is used for the projection of the matrices in the Cartesian space. However, due to the nature of a 7-DoF manipulator, the Jacobian is not a square matrix and thus not invertible. To address this limitation, several techniques can be applied, including pseudoinverse

methods [Corke, 2017]. These approaches allow for approximations of the inverse solutions.

As will be discussed in the following chapter, in terms of implementation, both dimensions are mixed since τ are the control inputs and F are the forces estimated from the sensed torques.

2.5 Control Design

Depending on the number of variables that characterize the manipulator, robots can be considered redundant or non-redundant. If the number of variables is higher than the number of degrees of freedom needed, they are considered redundant. When this happens, the robot arm can reproduce different joint configurations while keeping its tool center point of the end effector in the exact same position and orientation. This control situation is called nullspace motion and becomes very useful in some situations, as for example moving the robot arm joints to avoid a collision without displacing the end effector [Salt Ducaju et al., 2021]. As mentioned before, during the formulation of the controller equations in this section, friction will not be considered due to the nonlinearities that it brings [Ott, 2008].

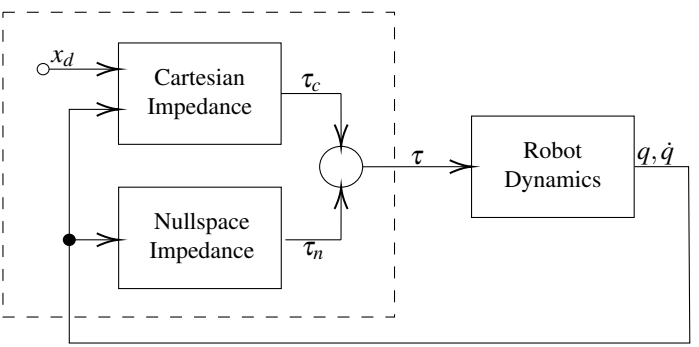

Figure 2.2 Block diagram of the control design [Ott, 2008].

The control design follows the block diagram shown in Figure 2.2, where the Cartesian impedance and the nullspace one are combined through the superposition principle

$$\tau = \tau_c + \tau_n \tag{2.9}$$

where τ_c represents the Cartesian impedance, τ_n the nullspace impedance and τ the commanded joint torques. x_d represents the desired position in Cartesian coordinates.

Cartesian Impedance

The first step to define the Cartesian impedance as a mechanical system is formulating the external forces F_{ext} from the environment as a function of desired inertia, damping and stiffness [Ott, 2008]. These external forces can be written in Cartesian space as

$$F_{ext} = M_d\ddot{x}_e + D_d\dot{x}_e + K_d x_e \tag{2.10}$$

$$x_e = x - x_d \tag{2.11}$$

where $M_d \in \mathbb{R}^{n\times n}$, $D_d \in \mathbb{R}^{n\times n}$, and $K_d \in \mathbb{R}^{n\times n}$ are the desired inertia, damping, and stiffness matrices, respectively. x_e represents the deviation from the desired position, x_d.

Substituting Equation (2.10) into Equation (2.7) and rewriting the expression, the control law obtained is [Ott, 2008]

$$\tau_c = g(q) + J^T(q)[M_x(x)\ddot{x}_d + C_x(x,\dot{x})\dot{x}_d - K_d x_e - D_d\dot{x}_e] \tag{2.12}$$

As can be seen in Equation (2.12), the external forces are no longer part of it. This becomes very convenient since the external forces cannot be measured directly. It is important to mention that to achieve this solution, the desired inertia has been equalized with the robot inertia ($M_d = M_x$).

Stiffness. The stiffness matrix is built according to the expected actions of the robot. If a good trajectory accuracy is required, the values must be larger. Otherwise, if the idea is to anticipate and reduce a possible impact, smaller values should be set. In summary, the stiffness matrix represents an exchange between accuracy and contact force.

It is composed by stiffness submatrices as follows

$$K_d = \begin{pmatrix} K_t & K_c \\ K_c & K_r \end{pmatrix} \tag{2.13}$$

where K_t, K_r and K_c are the translational, rotational and coupling stiffness submatrices, respectively.

Damping. The damping matrix is designed to achieve an optimal transient behaviour in the robot motion. The coefficients are generally chosen following those of the stiffness matrix K_d but can vary depending on the desired response. The definition of the damping matrix is [Ott, 2008]

$$D_d = 2Q^T D_\xi \sqrt{\lambda_K} Q \tag{2.14}$$

where $Q \in \mathbb{R}^{n\times n}$ is a non-singular matrix, D_ξ is a diagonal matrix with damping factors $\xi \in [0,1]$ on its diagonal, and $\lambda_K \in \mathbb{R}^{n\times n}$ is a diagonal matrix composed of

the generalized eigenvalues of K_d.

The values of ξ that make up D_ξ represent the damping ratio, *i.e.*, how much energy stored in the oscillation is dissipated. Values tending to 1 will reduce the overshoot and give a fast response, while values close to 0 will dissipate energy slower and, therefore, produce a more oscillatory answer from the robot.

Null-Space Impedance

There are many ways of defining the nullspace impedance control law. The way followed in this explanation will be the one called the nullspace projection approach. In order to build the control equation for the nullspace impedance, the joint-space impedance τ_0 is first defined as [Ott, 2008]

$$\tau_0 = -D_n\dot{q} - K_n(q - q_{d,n}) \tag{2.15}$$

where $D_n \in \mathbb{R}^{n\times n}$ represents the desired damping matrix and $K_n \in \mathbb{R}^{n\times n}$ the desired stiffness matrix, both in the nullspace motion; while $q_{d,n}$ is the desired nullspace configuration that ideally satisfies the relation $f(q_{d,n}) = x_d$. Together with this, the nullspace impedance can be defined as

$$\tau_n = P(q)\tau_0 \tag{2.16}$$

where $P(q)$ represents a projection matrix built so that the Cartesian impedance τ_c can be dynamically separated from the joint-space impedance τ_0. $P(q)$ can be defined as [Ott, 2008]

$$P(q) = I - J^T(q)[J(q)M^{-1}(q)J^T(q)]^{-1}J(q)M^{-1}(q) \tag{2.17}$$

The nullspace impedance control law would be obtained by substituting Equation (2.15) and Equation (2.17) in Equation (2.16).

2.6 Friction

Friction is the force or torque that opposes the motion when two surfaces slide or interact between them [Corke, 2017]. It is present in any rotating machinery, motor, or gearbox, such as those that robot joints possess. The net torque τ' that is obtained from a motor would be the motor torque τ_m without the friction value τ_f

$$\tau' = \tau_m - \tau_f \tag{2.18}$$

The friction torque can be modelled as a function of the rotating velocity

$$\tau_f = B\omega + \tau_C \tag{2.19}$$

where $B > 0$ is the viscous friction coefficient which also represents the friction slope (see Figure 2.3), and the offset τ_C is the Coulomb friction. The Coulomb friction is often modeled by the nonlinear function

$$\tau_C = \begin{cases} \tau_C^+ & if \quad \omega > 0 \\ 0 & if \quad \omega = 0 \\ \tau_C^- & if \quad \omega < 0 \end{cases} \tag{2.20}$$

Real systems usually present asymmetries between positive and negative values [Corke, 2017]. These asymmetries are more notorious for Coulomb friction than for viscous friction, and they depend on the direction of rotation. The sources of friction that a motor suffers from are various, as it could be its bearings, its gearbox, or a combination thereof.

Coulomb friction has a strong non-linearity and can cause difficulty when using numerical integration routines to solve the forward dynamics [Corke, 2017]. This is usually manifested by very long integration times.

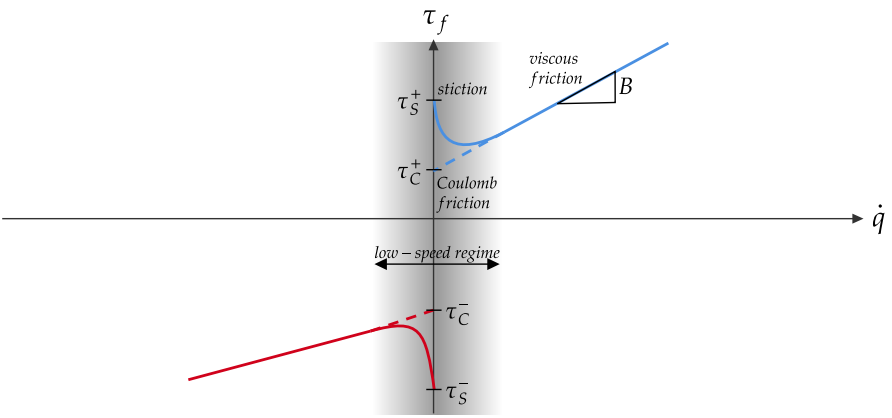

Figure 2.3 Joint motors' friction model and its components, plotting friction torques versus rotational speed [Corke, 2017].

Figure 2.3 shows the friction torque and its components, which have been described, against the rotational velocity. Notice the gray-shaded part of the plot, which indicates the low-speed zone. The curvature behaviour that appears in this gray-shaded part, between stiction (τ_S) and viscous friction, is called the Stribeck curve [TriboNet, 2023]. The Stribeck curve is a fundamental concept in tribology and lubrication fields, and represents the friction behavior in lubricated contacts as a function of viscosity of the lubricant, speed and roughness. This curve is generally described by three regimes of lubrication: full film lubrication regime (FF), mixed

lubrication regime (ML) and boundary lubrication regime (BL) [TriboNet, 2023]. These regimes are categorized by a parameter known as lambda ratio (λ).

Static Friction

When working in low-speed regimes, joint motors experience a phenomenon called static friction, also known as stiction [Corke, 2017]. This effect was discovered after Coulomb theory since there the friction experienced at these low velocities was greater than expected. As soon as the speed regime increases, the stiction starts disappearing and the viscous friction takes the lead. These torques that static friction impose on the robot joints will be named as **stiction bands** from now on. The stiction bands are generally asymmetric, having a different value between positives and negatives, and would be approximately equivalent to τ_S^+ and τ_S^- from Figure 2.3. These bands represent the torque values that must be characterized to achieve the optimal amplitudes for building the dithering signals.

Stiction, as will be demonstrated in Chapter 4, depends not only on the velocity but also on the torque load under which the joints are. Modeling and compensating the stiction phenomenon is the main objective of this thesis.

2.7 Dithering

A dithering signal is a small, repetitive motion that is superimposed on the control signal of a robotic joint [Stolt et al., 2015]. The purpose of the dithering signal is to help alleviate static friction, which is part of the friction that appears between surfaces in contact at low-speed regimes, and can result in stick-slip motion and decreased accuracy in robotic systems.

When a dithering signal is applied to a robotic joint, it can cause the joint to continuously move slightly, even when it is at rest. This shaking effect helps to break up the torque thresholds that may have been built up between the surfaces in contact while at low velocities and reduces the apparition of stiction occurring during normal operation. As a result, the end effector can move more smoothly and accurately, with reduced friction and improved reliability, even though the robot arm might exhibit more vibrations on the actuators.

A dithering signal can be modeled mathematically using a simple periodic function such as a sine or cosine wave. The amplitude and frequency of the dithering signal can be tuned according to the particular application for each of the joints and the desired level of stiction relief, which would be equivalent to the joint stiction bands. The construction of the dithering signals also depends on the joints' behaviour. For instance, a larger amplitude may be necessary to effectively break up higher levels of stiction, while a lower frequency may be sufficient for systems with lighter loads.

At the same time, an amplitude value that far exceeds the static friction bands could not only break up the stiction levels but also produce a shaking effect on the joints and end effector, reducing the accuracy of the trajectories or even being hazardous for the joint motors. A dithering signal $d(t)$ can be modeled as

$$d(t) = A\sin(2\pi ft) \tag{2.21}$$

where A is the amplitude of the dithering signal, f is the frequency, and t is the time.

In addition to a simple sine or cosine wave, other types of dithering signals, such as random signals or chirp signals, can also be used to model the dithering signal. The choice of signal type and the parameters' tuning will depend on the specific application and the desired level of performance.

In summary, a dithering signal can be an effective solution for the joint stiction problem because it helps to break up and reduce stiction existent in robotic joints. By continuously adding a small repetitive motion to the control signal, the robot arm is able to move more accurately, leading to improved performance and reliability.

3

Implementation

In this chapter, all the information about robot setups and software interfaces will be detailed, as well as all the steps followed in the applied approach.

3.1 Robot Setups and Software Interfaces

Hardware

LBR iiwa. The LBR iiwa robot is a 7-DoF manipulator designed by the company KUKA AG, as can be seen in Figure 1.1. The LBR iiwa is a collaborative robot arm, that is, meant to work in the presence of human interaction. It is designed with 7 axes, a maximum range of 80 cm, a weight of around 20 kg, and a maximum payload of approximately 7 kg for its end effector. This robot arm stands out because of its high accuracy and capacity to acknowledge the environment response, making it reliable to work in human-robot collaboration tasks [*LBR iiwa | KUKA AG* 2023].

The LBR iiwa includes independent actuators in each of its joints and provides different control modes such as torque, velocity and position control. In addition, it has sensors in each joint that give feedback on the torques in the joints.

A very useful feature provided by KUKA is the teach pendant known as *smartPAD*, which runs on the also included operating system software *Sunrise.OS* [*LBR iiwa | KUKA AG* 2023]. The *Fast Robot Interface* (FRI) enables access to the robot controller from other packages such as *iiwa_ros* [Chatzilygeroudis et al., 2019], allowing integration with ROS. The smartPAD allows for manual control and safety actions, as well as information about the joints, such as their applied torques or their positions.

The LBR iiwa arm assembly in the laboratory workspace, including the *smartPAD*, can be seen in Figure 3.1a. The LBR iiwa arm is mounted on a metal holder together with another arm of the same kind, which will not be used during this project.

Because of this setup, the robot arms bases are inclined. There is a *smartPAD* connected to each of the arms, as well as a different controller for each of them. It is important to mention the proximity of walls and the second arm, as well as a working table close to the LBR iiwa, which must be taken into account when conducting experiments.

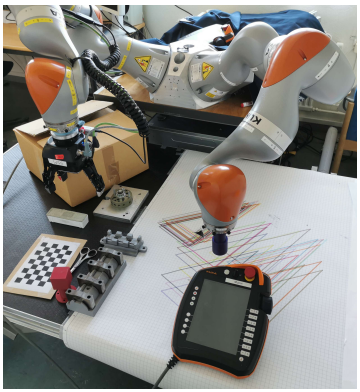

(a) LBR iiwa arm.

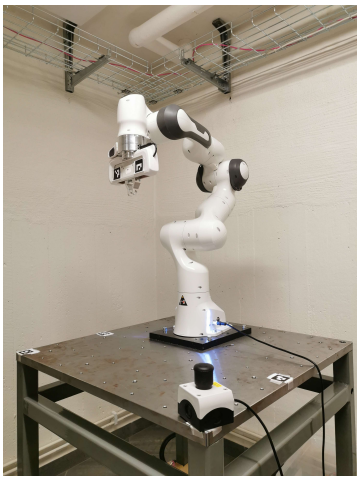

(b) Panda arm.

Figure 3.1 Robot setups and workspaces used for the thesis work.

Panda Arm. The Franka Emika robot, also known as Panda arm, is another 7 degree-of-freedom collaborative manipulator manufactured by the German company Franka Emika. The robot's weight is about 17.8 kg, with torque sensors equipped in each joint allowing for high precision with a maximum range of more than 85 cm, while its end effector can handle payloads of up to 3 kg [*Franka Emika Robot's Datasheet* 2023]. The Panda is designed to be collaborative, meaning it can work alongside humans in shared workspaces thanks to its built-in safety features, such as force sensing and collision detection. It is also often used for research purposes due to its high precision and manageability [*Franka Emika Robot's Instruction Handbook* 2023]. Figure 3.1b shows the setup and workspace for the Panda arm used during the thesis work. As can be seen, the setup also includes an emergency stop button.

The Panda arm is known for its user-friendly interface and software, including `Desk`, which is the browser-based user interface where entire tasks can be set up without prior programming knowledge. However, the Panda also offers `Franka Control Interface` (FCI) [*Franka Emika Github* 2023], which allows a fast and direct low-

level bi-directional connection to the manipulator at 1 kHz. The FCI can be accessed via several open-source components such as:

- `libfranka`, a C++ library that provides low-level control and API gaining access to the robot state and model library to compute the desired kinematic and dynamic parameters.
- `franka_ros`, integrates `libfranka` into ROS and ROS control making it possible to use ROS as a middleware.

Software

ROS. ROS stands for *Robot Operating System* and is an open-source framework used for robot systems [Quigley et al., 2009]. It consists of a set of software libraries and tools that make it easier to create robot applications. It is meant to be flexible, modular, and scalable, making it easy to integrate various hardware and software components into a robotic system.

At a high level, ROS consists of a set of *nodes*, which are processes that perform computations, that communicate with each other by sending and receiving messages over ROS topics. ROS messages are simple data structures that contain the necessary information, and ROS topics are the *channels* over which messages are exchanged between nodes. Nodes can publish messages to a topic and/or subscribe to receive messages from a topic. When a message is published on a topic, all nodes that subscribe to that topic receive a copy of the message. Nodes can be written in different programming languages, where the two most common ones are Python and C++, and still be able to communicate with each other.

There are many different kinds of software libraries, or packages, in ROS that makes developing easier and more convenient. The ROS package for managing controllers is called `ros_control` [Chitta et al., 2017]. It provides a set of tools and interfaces to create and manage robot controllers in ROS, allowing for switching between different controllers in real time.

In addition to packages, there are also other tools and plugins that are relevant for this thesis such as:

- `rqt_reconfigure` is a ROS plugin that provides a GUI for dynamically reconfiguring parameters for different ROS nodes if they support dynamic reconfiguration [*rqt_reconfigure* 2023]. This allows, for example, real-time changes in the stiffness of the *Cartesian Impedance Controller*.
- `Gazebo` is a simulation environment for robotics [Koenig and Howard, 2004]. It allows developers to create and test robot models in a virtual environment

before deploying them on physical hardware. Gazebo can simulate a wide range of robot sensors, actuators, and environments, making it a powerful tool for testing and debugging robot software.

- `RViz` is a 3D visualization tool for ROS [*Rviz Visualization Tool* 2023]. It allows developers to view and interact with robot models, sensor data, and other visualizations in real-time. RViz can be used for tasks such as debugging robot software, visualizing sensor data, and creating custom user interfaces for robot applications.

- `MoveIt` is a software framework for motion planning and control in ROS [Coleman et al., 2014]. It provides a set of libraries and tools for creating motion plans for robot arms, grippers, and other manipulators. MoveIt can be used for tasks such as trajectory planning, obstacle avoidance, and grasping.

Cartesian Impedance Controller. The controller used in this project is a *Cartesian Impedance Controller* provided and developed by the thesis supervisors Matthias Mayr and Julian M. Salt-Ducaju. It is a C++ implementation and offers some key features such as being able to dynamically change the reference poses, Cartesian stiffness, and nullspace configurations. The base library can be integrated with other software; however, it also implements a `ros_control` controller on top of the base library so that it can be integrated with ROS [Mayr and Salt-Ducaju, 2022].

3.2 Approach and Method

In this section, the approach and method used for the project will be presented and explained. The different experiments that make up the whole process realized during the thesis work were applied to both robot arms, following the same order and steps.

The aim of the thesis is based on identifying and mitigating the existing stiction inside the joints. Stiction will be represented by stiction bands with specific values for each of the joints that each of the robot arms has. Once this goal is achieved, the stiction relief will be implemented as a dithering signal in different trajectories so the pose deviations during trajectories are reduced.

Two approaches were designed to find these stiction bands. The first approach could be considered theoretical, since it brings data from identification trajectory experiments and processes it applying the dynamics equations in order to get friction torque values. These friction torques are calculated from the dynamics equations using the parameters of the robot states (q, $\dot{q}$, $\ddot{q}$ and τ) and are then used to obtain a friction model of the robot joints using the Least Squares Method (LSM) [Miller, 2006]. The second is an empirical method that was named Single Joint

Experiment (SJE). SJE is based on iterative motions in each rotational direction, *i.e.*, positive and negative, in different load configurations, for each of the robot arm joints. Both approaches are possible and valid, although the results obtained from the first method were unreasonable and the ones used were those of the SJE, as will be seen in Chapter 4.

Generated Trajectory Experiment

Before performing the dynamics identification and SJE approaches, some trajectory planning was practiced. These experiments will be called Generated Trajectory Experiment, abbreviated as GTE. The results obtained from these experiments will be further used as a base sample to compare between real robot trajectories with and without applied dithering. Using the *Cartesian Impedance Controller*, simple point-based trajectories were realized, creating regular polygons in 2D such as a triangle or a pentagon with the end effector. The *Cartesian Trajectory Generator*[1] generated the Cartesian linear paths between poses that would recreate these polygons. These generated trajectories follow a constant acceleration and deceleration profile until the maximum rotational and translational velocities are reached. The acceleration, deceleration, and velocity values of the trajectories are user-defined, allowing customization based on specific requirements.

Once the trajectories were created, they were tested in simulation, checking the robot response through `Gazebo` and `RViz` as shown in Figures 3.2a and 3.2b respectively. As a procedure, every trial or experiment was first implemented in simulation as a safety check to see the robot's response.

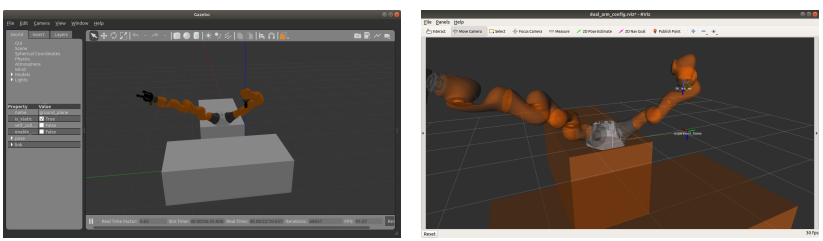

(a) `Gazebo`. **(b)** `RViz`.

Figure 3.2 LBR iiwa arm in both `Gazebo` and `RViz` environments used for simulation.

After trying different simulation trajectories and learning the security measures available in the *smartPAD* for the LBR iiwa, the trajectories were realized using the real robot. The *Cartesian Impedance Controller* was the controller implemented

[1] `https://github.com/matthias-mayr/cartesian_trajectory_generator`

during these experiments, sending to it the start and goal poses generated by the *Cartesian Trajectory Generator*. It is important to mention that the trajectory points are formulated relative to a base frame, which simplifies the overall motion planning process and allows for easy adjustments of the trajectory's location when needed. The procedure for GTE is schematically illustrated in Figure 3.3.

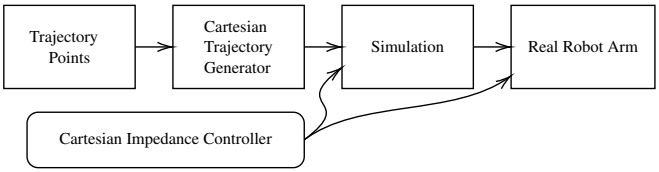

Figure 3.3 Schematic illustration of the GTE steps.

These 2D polygonal trajectories were also implemented in the Panda arm, but first in the simulation environment shown in Figures 3.4a and 3.4b. For this experiment, the main difference in implementation between both robot arms lied in the use of the smartPAD, since Panda did not have it.

Both in simulation and reality, and for each of the robot setups, the trajectories were repeated a defined number of iterations. Between these iterative trajectories, the average error and standard deviation of each experiment was calculated. In order to ensure consistency and repeatability between iterations, a reset function was developed. This reset function was designed to set the robot arm in that same arbitrary configuration before any trajectory iteration started, and was built using forward kinematics together with setting a nullspace stiffness and configuration.

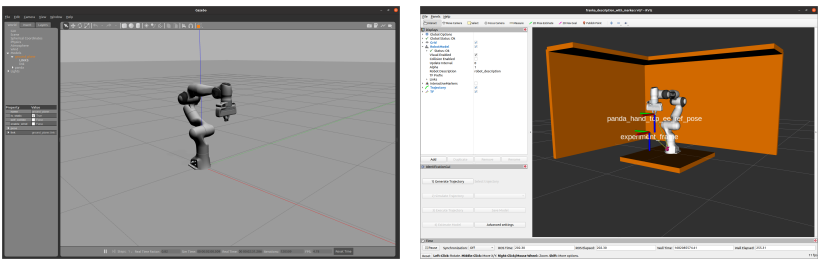

(a) `Gazebo`. **(b)** `RViz`.

Figure 3.4 Panda arm in `Gazebo` and `RViz`.

Stiction Characterization

Dynamics Identification. To obtain a starting value for the stiction bands as mentioned in Section 2.6, an identification of the dynamics of the robot was performed. This was initially done with a package called `ROSdyn`[1], which is used for dynamics identification and works with `MoveIt!` to generate identification trajectories. It also records all robot states required for identification. It can estimate the viscous and Coulomb frictions, as well as elements of the inertia matrix. However, the mass, viscous friction and inertia values obtained were unreasonably high and, despite extensive debugging efforts, a different approach was decided. Instead of relying on a third-party library for identification, the same generated trajectories were used and the recording of the necessary robot states was done by subscribing to ROS topics.

From Equation (2.4), the friction torques τ_f can be obtained if the rest of the parameters are provided. With the Panda robot, `libfranka` provides a robot model library where dynamics parameters such as the inertia matrix M, the Coriolis / centrifugal matrix C and the gravity vector g can be obtained. This can be done either in real time, or offline.

Using the recorded samples, the friction torques τ_f were extracted and plotted against the velocity $\dot{q}$, resulting in a graph similar to Figure 2.3. The **Least Squares Method** [Miller, 2006] was used to fit the measured data using Equation (3.1) where m is the slope of the trend line, b is the intercept with the y-axis and N is the amount of samples.

The results were divided into positive and negative velocities, and the intercept value of each trend line with the y-axis served as the initial stiction band values (τ_S^+ and τ_S^-).

$$
\begin{aligned}
m &= \frac{N\sum(\dot{q}\tau_f) - \sum\dot{q}\sum\tau_f}{N\sum\dot{q}^2 - (\sum\dot{q})^2} \\
b &= \frac{\sum\tau_f\sum\dot{q}^2 - \sum\dot{q}\sum(\dot{q}\tau_f)}{N\sum\dot{q}^2 - (\sum\dot{q})^2}
\end{aligned}
\tag{3.1}
$$

Single Joint Experiment. The Single Joint Experiment (SJE) is an empirical and quantitative test that aims to find the minimum torque to move a joint from a static position. Stiction appears in low-speed regimes, mainly at velocities close to zero. Furthermore, the stiction values may vary depending on the amount of load

[1] `https://github.com/CNR-STIIMA-IRAS/rosdyn`

applied to the specific joint that is being analyzed and generally present asymmetries between positive and negative joint rotations. The SJE was designed taking these conditions into account. Following the procedure schematically represented in Figure 3.5, each joint was focused on individually. The robot arm was moved to a specific configuration using the *Cartesian Impedance Controller*, in which the joint studied was under a maximum or minimum load value. The robot arm was allowed a maximum deviation of 0.1 radians for each of the joint positions from the desired joint configuration. Once the robot arm was in this desired joint configuration, iterative motions in both directions of rotation started. The motion consisted of sending an increasing torque by small steps from zero to this specific joint until a set threshold of position difference was reached. This was done with a torque controller which allowed the torques to be sent to individual joints. This method was repeated for the same configurations with a defined number of iterations for both the positive and negative directions.

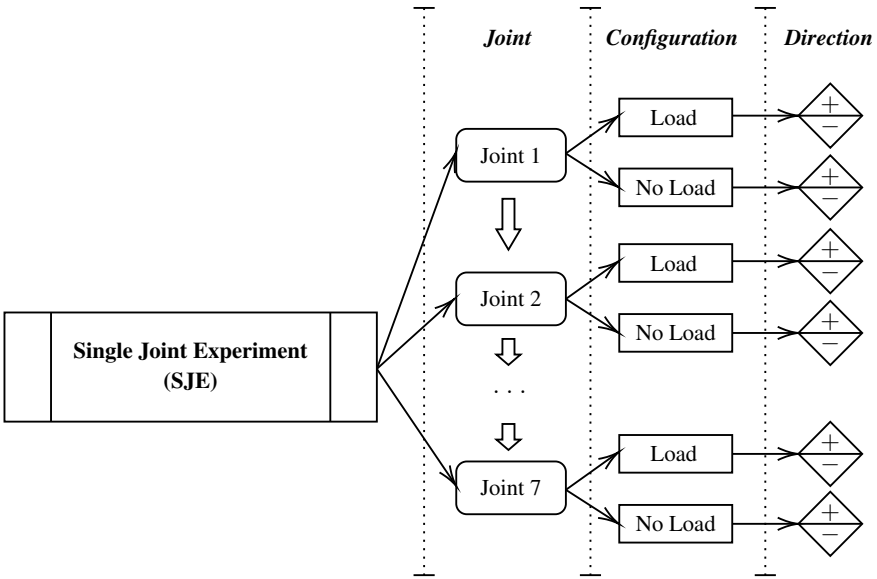

Figure 3.5 Schematic illustration of the SJE steps, first focusing on an individual joint, for a specific load configuration and both rotation directions, repeating the experiment motion a defined number of iterations.

As has been said, the robot arm is moved to a predetermined configuration in which the joint that is being analyzed is under a maximum or minimum load value. These specific configurations were found by setting the Cartesian stiffness to zero, so the robot arm acquires a free-motion state in which it can be moved manually. The robot was then placed in several poses while reading the sensed torque values to find

a maximum or minimum in its joints. The sensed torques were taken into account as absolute values, which means that the maximum data read could be positive or negative, while the minimum values were the closest to zero possible. Following this procedure, a list of poses that would guarantee the load situation in each case for each joint was created.

As a stopping condition for each experiment's iteration, it was proposed to put a threshold on a variable of interest that described the robot state. Due to the joint under analysis receiving an increasing torque (in absolute terms) and the velocity being a variable of interest when finding stiction, the first threshold implemented was based on a maximum velocity value. Whenever the robot arm joint exceeded this velocity threshold, the reset script would bring it to the defined configuration to start the next iteration. However, this threshold ended up not being reliable during some attempts, where the robot arm would never reach the velocity check and continued rotating. As a consequence, it was decided to change the velocity variable to position, which was also a variable of interest. The threshold was then set to a maximum joint angular variation (from the starting joint angle of the configuration) of 0.15 radians, which is around 8.6º.

The robot's motion depends on the Cartesian stiffness values. A specific trajectory that starts from the exact same joint configuration but is executed with different stiffness values, will yield different results. For this reason, various stiffness values were tested during the experiments, which will be discussed in further detail.

As well as in the Generated Trajectory Experiment (GTE), the results obtained during this experiment will serve as a baseline to compare with the results after applying dithering. This comparison will be done in the next chapters.

During the application of this method to the LBR iiwa robot arm, some difficulties came up. Calibration issues in the joint torques and the gravity compensation caused the robot arm to fall down at some specific configurations, which meant non-valid data. The solution consisted of reading the external torques in the joints for some seconds before the iterations started, using the average of these joint torques as a new start torque instead of zero. This phenomenon was not observed during the experiments with the Panda arm.

Dithering Experiments

After completing the experimental setups and obtaining a set of preliminary stiction band values, the next step was to implement dithering. As detailed in Section 2.7, a periodic torque signal τ_{dith} of the form Equation (2.21) was added to the controller commanded torque τ, where the amplitude A was equal to the stiction value obtained, f was initially an arbitrary frequency, and t represented the time in seconds obtained from ROS. Equation (3.2) shows how the dithering torque signal is added to the commanded torque of the controller:

$$\tau_{total} = \tau + \tau_{dith} \tag{3.2}$$

where τ_{total} represents the torques received by the robot, τ the commanded torques of the controller and τ_{dith} the dithering torque signals.

For the SJE experiment, the dithering signal was applied to the torque controller, whereas for the GTE experiment, it was applied to the *Cartesian Impedance Controller*. Based on the stiction values obtained from dynamics identification and the values obtained from SJE, a set of base dithering amplitudes were established. When implementing dithering in the *Cartesian Impedance Controller*, it was critical to do so prior to any additional processing or modifications to the commanded torques, as maintaining the safety features was a top priority.

The SJE experiment was subsequently conducted multiple times with various scale factors on the amplitudes, each with different sets of frequencies, to determine the best amplitudes and frequencies for each joint that resulted in the greatest reduction in torque required to reach the threshold. These sets of amplitudes and frequencies were also used for GTE and the results were then compared to the non-dithering results.

4

Results

The primary results of this thesis focused on the beneficial impact of dithering on the accuracy of the robot's motion. First, the results of the stiction characterization and the dithering signal's construction are presented, since the different dithering signals were built once the stiction bands were modeled. Then, the implementation of dithering and how it improved the experiments are shown.

4.1 Stiction Characterization

The modeling of the stiction in the robot arms and the methods followed to obtain it will first be described in detail. Modeling of the robot dynamics was used to characterize the stiction bands present in each of the joints. The two main approaches, as introduced in Section 3.2, were initially followed. However, the results from the dynamics identification and the LSM approach turned out being unreasonable, and the results obtained from the SJE method were used instead.

Dynamics Identification

The initial approach consisted of complex trajectories created by the library `RosDyn` using `MoveIt!`. These trajectories are meant for identification and, thus, for exploring the whole workspace of the robot. The trajectories were run with the *Cartesian Impedance Controller*, and as a safety measure, the arm was not excited to its full speed.

The dynamic model obtained from the library `RosDyn` showed unreasonable results, as they differed substantially from the expected values. This includes the appearance of negative values of the link masses and abnormally high values of inertia and viscous friction in the joints, which can be observed in Table 4.1.

As the above-mentioned approach failed to deliver an accurate dynamic model of the robot arms, an alternative method was developed, but only for the Panda arm.

Table 4.1 `RosDyn` model results for the LBR iiwa.

Joint	Mass (kg)	CoM_X (m)	CoM_Y (m)	CoM_Z (m)	Coulomb (Nm)	Viscous (Nms)
1	3.45	0.0313	-0.0340	0.1200	-0.22	-128,728.04
2	3.48	0.0293	-390.1560	0.0380	-0.05	202,673.10
3	-50.15	-0.0001	-0.0023	-16.8125	-0.09	-2.69
4	298.57	-0.0002	-0.8074	0.0003	-0.59	9.31
5	260.03	-0.0004	-0.0468	-0.4349	-0.35	-1.93
6	249.22	0.0004	-0.0772	0.0120	-0.28	0.30
7	249.02	0.0000	0.0000	-0.0669	-0.32	0.76

Joint	Mass (kg)	I_{XX} (kgm^2)	I_{XY} (kgm^2)	I_{XZ} (kgm^2)	I_{YY} (kgm^2)	I_{YZ} (kgm^2)	I_{ZZ} (kgm^2)
1	3.45	0.02	0.00	0.01	0.00	-0.01	-7,227.83
2	3.48	-535,461.00	-40.01	0.00	-1,818.20	-51.57	-519,401.00
3	-50.15	16,383.70	0.10	-0.22	17,206.30	-2.06	-822.79
4	298.57	369.28	0.14	0.06	822.61	-0.01	-453.63
5	260.03	78.60	-0.02	0.10	127.42	7.62	-49.13
6	249.22	30.36	0.07	-0.12	47.85	0.98	-17.37
7	249.02	6.89	0.00	0.01	6.91	-0.01	-0.48

Since the library `libfranka` can directly provide the inertia and Coriolis matrices of the Panda arm, these did not need to be estimated, and therefore it was no longer necessary to obtain the inertia components from identification. The friction torques τ_f were extracted by reorganizing the Equation (2.4) and substituting the matrices and measured torques.

Least Squares Method. Once the friction torques τ_f were calculated, the stiction bands τ_S of the various joints could be approximated using the Least Squares Method (LSM). Friction torques and joint velocity values of a given trajectory were used to generate a list of values τ_f and $\dot{q}$, which were expected to exhibit behavior similar to that depicted in Figure 2.3. LSM was then used to calculate the intercept, which provides an approximation of the stiction bands τ_S. Although a suitable data set was found for joint 7 of the Panda arm, as shown in Figure 4.1a, no such set was identified for the remaining joints, as demonstrated in Figure 4.1b. Friction-velocity plots for each joint of the Panda arm can be found in the Appendix A.

The LSM results obtained from the two data sets are presented in Table 4.2. The parameter *Intercept* represents the y-axis intercepts of the LSM trend lines, indicating the approximate positive and negative values of the stiction bands τ_S^+ and τ_S^-, respectively. Notably, the correlation coefficients R^2 were generally low, particularly for joint 1. The values for the rest of the joints can also be found in Appendix A.

Table 4.2 LSM results for joints 1 and 7 separated by positive and negative direction.

	Joint 1 (+)	Joint 1 (-)	Joint 7 (+)	Joint 7 (-)
Intercept	0.81	-0.2150	0.5576	-0.5395
Slope	-3.02	0.0440	0.1209	0.1198
R^2	0.00235	0.0000011	0.0299	0.0418

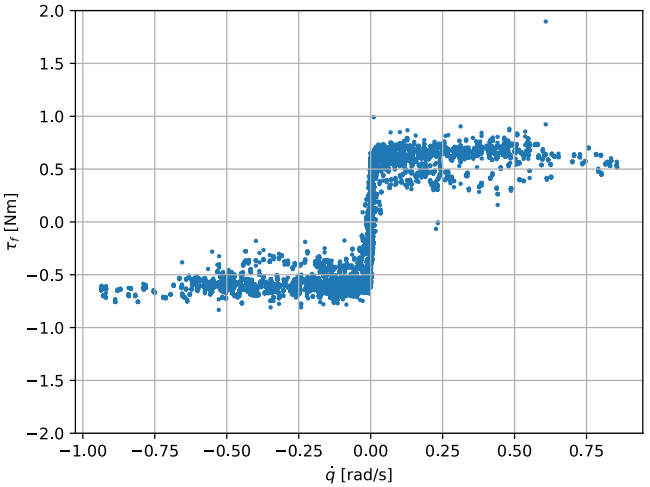

(a) Joint 7.

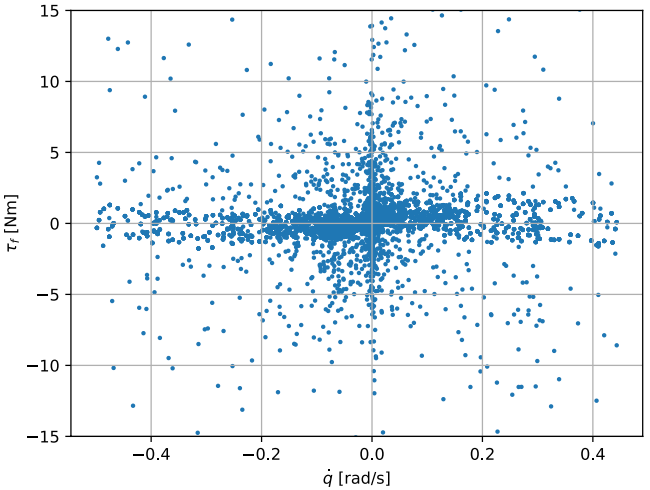

(b) Joint 1.

Figure 4.1 Two friction-velocity dataset plots extracted from the identification trajectories and dynamics equation to which LSM was applied.

Single Joint Experiment

The identification approach did not yield optimal results, as previously explained. However, the Single Joint Experiment (SJE) demonstrated consistency and proper repeatability between iterations. Despite some calibration issues with the LBR iiwa arm, the SJE provided promising results that could serve as a basis for designing the dithering signals.

Figures 4.2 and 4.3 illustrate some of the results from the SJE. The remaining graphs are shown in Appendices B and C. Each joint configuration is represented in a different plot, which is further divided into two subplots. The warm colors indicate the positive direction motions, while the cold colors represent the negatives. All commanded torques have been represented in absolute values for comparison purposes. The upper subplot depicts the robot's behavior in each iteration, while the lower subplot shows the mean and standard deviation of the iterations from the subplot above. To calculate the mean and standard deviation of the iterations, the last values from those iterations that passed the position threshold before others were extended until the last iteration ended ensuring the same amount of data points between all iterations. Note that the iterations did not end up at the same position value due to the allowed deviation of maximum 0.1 radians when moving the robot to the desired configuration.

Table 4.3 Minimum mean stiction torques extracted from the SJE, called *base* values or τ_b, for both robot arms.

Joint Configuration	*LBR iiwa τ_b (Nm)*	*Panda arm τ_b (Nm)*
Joint 1 Load (+)	0.3284	0.5711
Joint 1 Load (-)	-0.6265	-0.8287
Joint 1 No load (+)	1.072	0.85
Joint 1 No load (-)	-0.8724	-0.6501
Joint 2 Load (+)	0.6493	1.079
Joint 2 Load (-)	-1.265	-3.132
Joint 2 No load (+)	0.8497	0.9935
Joint 2 No load (-)	-1.241	-0.9143
Joint 3 Load (+)	0.7052	0.6549
Joint 3 Load (-)	-0.3797	-1.337
Joint 3 No load (+)	0.6067	0.7777
Joint 3 No load (-)	-0.7142	-0.6881
Joint 4 Load (+)	0.2813	1.664
Joint 4 Load (-)	-0.8843	-0.5261
Joint 4 No load (+)	0.9146	1.262
Joint 4 No load (-)	-0.5207	-0.5286
Joint 5 Load (+)	0.4223	0.4707
Joint 5 Load (-)	-0.8317	-0.7224
Joint 5 No load (+)	0.8106	0.5913
Joint 5 No load (-)	-0.523	-0.506
Joint 6 Load (+)	0.3675	0.4691
Joint 6 Load (-)	-0.5363	-0.3941
Joint 6 No load(+)	0.6835	0.3998
Joint 6 No load (-)	-0.6362	-0.4878
Joint 7 Load (+)	0.4289	0.6348
Joint 7 Load (-)	-0.3194	-0.6701
Joint 7 No load (+)	0.5358	0.604
Joint 7 No load (-)	-0.1826	-0.6314

Table 4.3 summarizes the results shown in Figures 4.2 and 4.3. It contains the average minimum torque values needed to reach the set position threshold, approximately equal to the stiction bands for each of the joint configurations. These values will be referred to as *base* values or τ_b henceforth, as they served as reference amplitudes to construct the best dithering signals. The values obtained after implementing the dithering signals will be generically called τ_{SJE}.

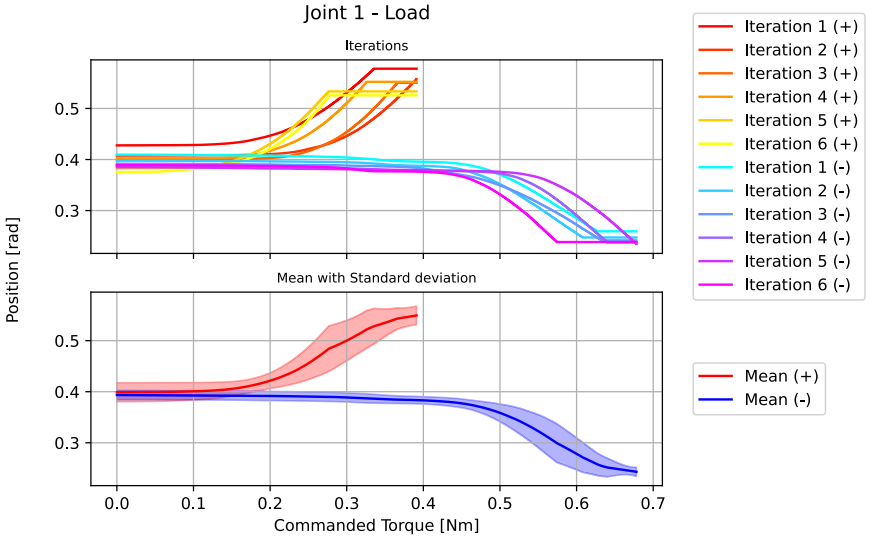

(a) Joint 1 Load configuration.

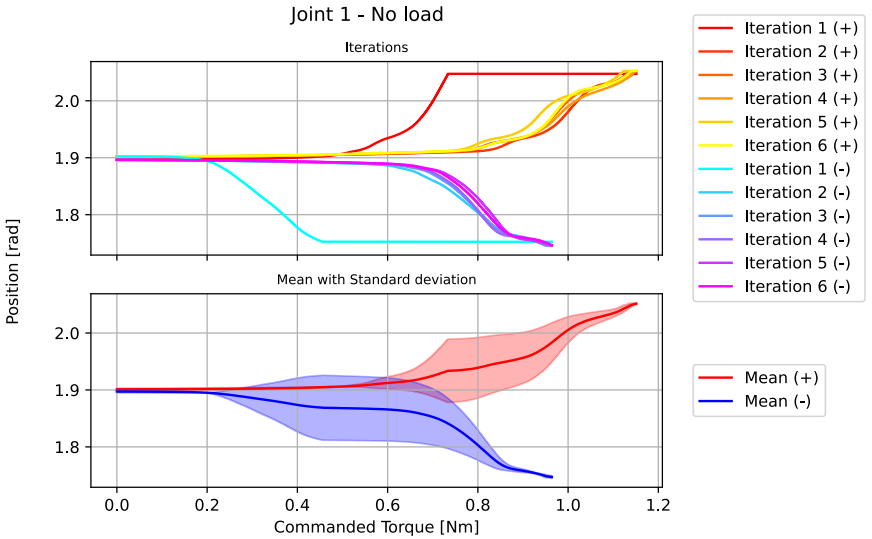

(b) Joint 1 No Load configuration.

Figure 4.2 LBR iiwa arm behaviour in SJE without dithering applied. The upper plot shows the iterations with the extended last values while the lower plot shows the iterations mean torque and standard deviation.

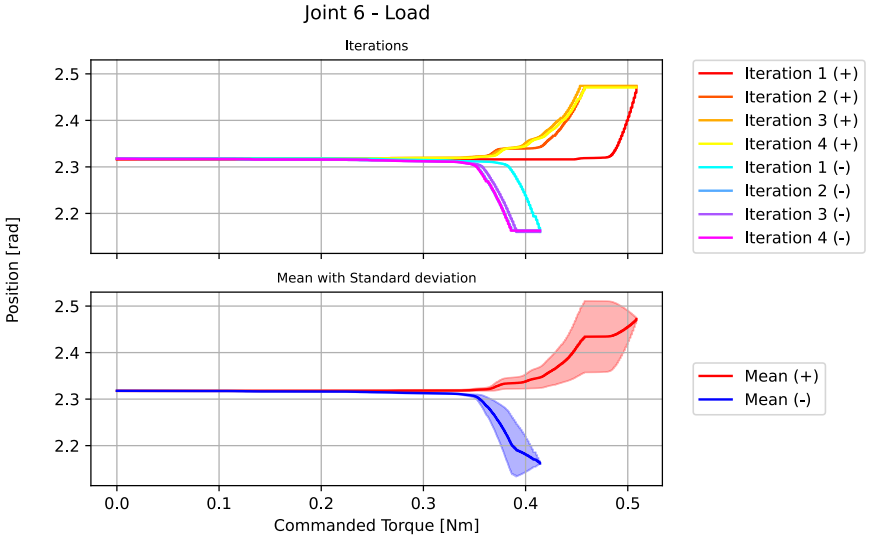

(a) Joint 6 Load configuration.

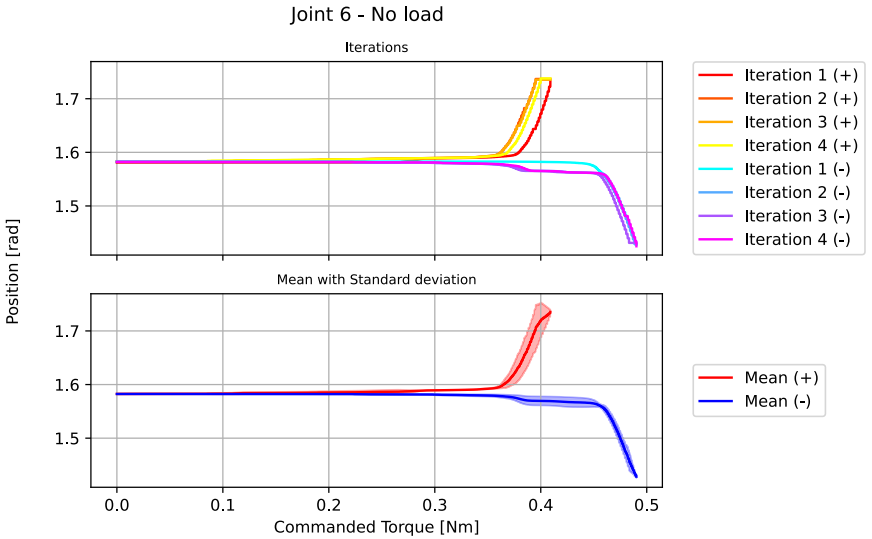

(b) Joint 6 No Load configuration.

Figure 4.3 Panda arm behaviour in SJE without dithering applied. The upper plot shows the iterations with the extended last values while the lower plot shows the mean torque and standard deviation.

Table 4.4 illustrates a comparison between the stiction characterization results from the LSM and the SJE. It can be appreciated that some values coming from the LSM are close to the ones from the SJE, as for example the positive intercept against the load and no load positive motions for joint 1, or both LSM values for joint 7 against the ones obtained from the SJE. Nevertheless, most of the results from LSM are unreasonable and away from the ones obtained in the SJE. As has been stated already before, the values that will be further used are the ones from the SJE.

Table 4.4 Comparison between LSM and SJE stiction characterization results.

Joint	Direction	LSM Intercepts	*Base* τ_b (Nm)	Load Configurations
1	+	0.8138	0.5711	Load
			0.85	No Load
	-	-0.2150	-0.8287	Load
			-0.6501	No Load
2	+	-3.1325	1.079	Load
			0.9935	No Load
	-	-4.1755	-3.132	Load
			-0.9143	No Load
3	+	1.0559	0.6549	Load
			0.777	No Load
	-	0.1632	-1.3377	Load
			-0.6881	No Load
4	+	3.4506	1.664	Load
			1.262	No Load
	-	2.7097	-0.5261	Load
			-0.5286	No Load
5	+	-0.0394	0.4707	Load
			0.5913	No Load
	-	-0.3908	-0.7224	Load
			-0.506	No Load
6	+	0.3740	0.4691	Load
			0.3998	No Load
	-	0.3907	-0.3941	Load
			-0.4878	No Load
7	+	0.5576	0.6348	Load
			0.604	No Load
	-	-0.5395	-0.6701	Load
			-0.6314	No Load

4.2 Dithering Experiments

Once the joint stiction modeling of the joints of the two robot arms was completed, dithering experiments were performed. The optimal amplitudes and frequencies for dithering were selected mainly based on empirical trial and error, considering the robot behavior feedback from the Single Joint Experiments (SJE).

Single Joint Experiment Improvement

As previously explained, dithering is intended to reduce the stiction effect on the joints of the robot arm, thus decreasing the minimum torque required to move the arm. The dithering signals were constructed on the basis of how different amplitudes and frequencies improved the results of the SJE. The frequency was the first variable that was modified to determine if improvements could be observed.

Different frequencies (20, 50, 100, and 200 Hz) were attempted on the SJE for the LBR iiwa robot arm. However, a consistent improvement pattern that provided reliable results could not be identified. Table 4.5 illustrates the minimum torque values required to reach the position threshold for joints 1 and 2 of the LBR iiwa robot arm after adding a 100 Hz dithering signal. This table, as well as the subsequent tables shown in this section, shows the difference between the base torque values and the new torque values as a percentage calculated in absolute values. A negative value indicates an improvement. To clarify this difference, green and red colors are used, with the former indicating improvement and the latter indicating the opposite.

Table 4.5 Stiction variation extract from the SJE in LBR iiwa with 100 Hz dithering.

Joint Configuration	*Base* τ_b *(Nm)*	τ_{SJE} *100 Hz (Nm)*
Joint 1 Load (+)	0.3284	0.3686 (+12.21%)
Joint 1 Load (-)	-0.6265	-0.7239 (+15.53%)
Joint 1 No load (+)	1.072	1.0887 (+1.56%)
Joint 1 No load (-)	-0.8724	-0.7538 (-13.6%)
Joint 2 Load (+)	0.6493	0.8542 (+31.57%)
Joint 2 Load (-)	-1.2646	-1.2192 (-3.59%)
Joint 2 No load (+)	0.8497	0.7785 (-8.38%)
Joint 2 No load (-)	-1.2411	-1.1674 (-5.94%)

An example of the SJE results for the LBR iiwa, which can be seen in Table 4.5 and Figure 4.4 shows the response of joint 1 of the LBR iiwa after implementing a dithering signal using the *base* values from Table 4.3 as amplitudes and a signal frequency of 100 Hz. Due to these unsatisfactory results and the time constraints, it was decided to continue working with the Panda arm setup instead.

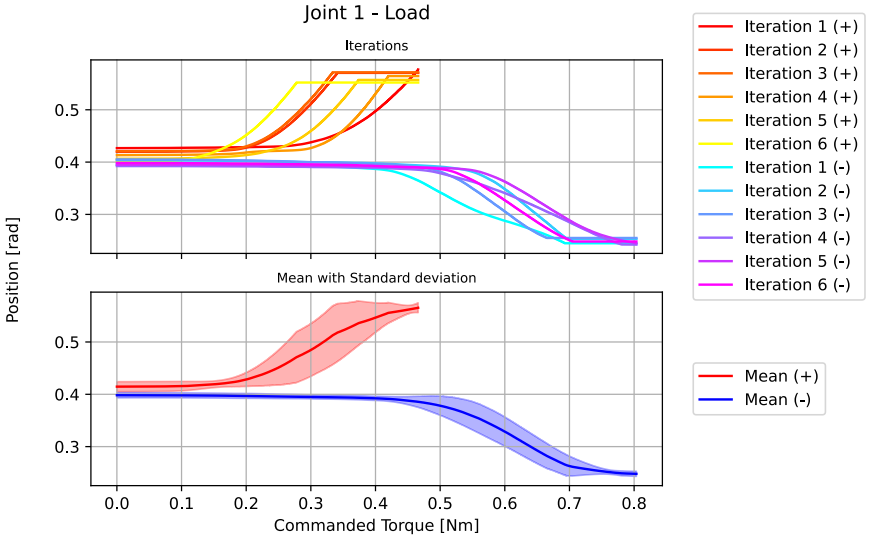

(a) Joint 1 Load configuration.

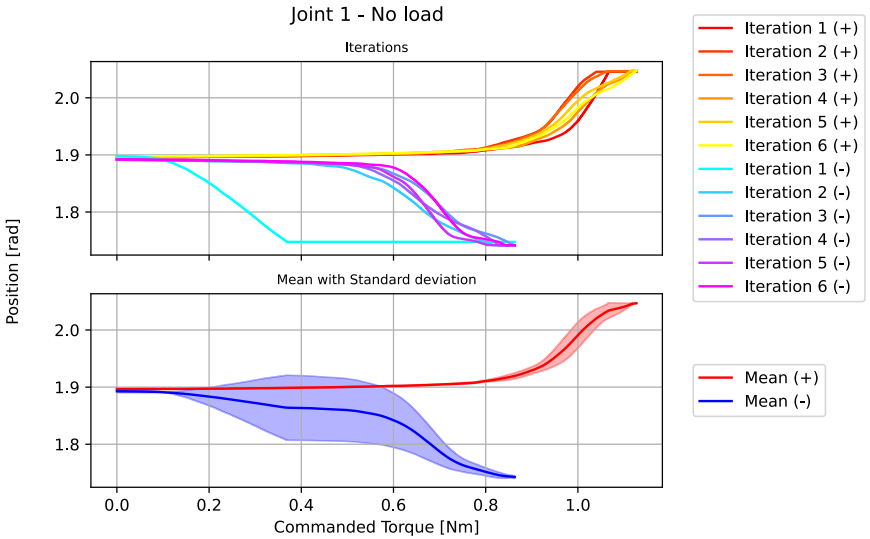

(b) Joint 1 No Load configuration.

Figure 4.4 LBR iiwa arm behaviour in SJE with 100 Hz and *base* amplitudes dithering applied.

The dithering signals were then applied to the SJE in the Panda arm using the base values of Table 4.3, as was done with the LBR iiwa arm. Frequencies of 80, 50, 30, and 15 Hz were used in these experiments. The results obtained were promising, but varied in the τ_{SJE} values obtained. Table 4.6 presents the dithered stiction torque values for each configuration and frequency. It can be observed that some frequencies improved the motion of a joint more than others, but the 80 Hz frequency was never the best among them. Therefore, the 80 Hz option was excluded in the following steps.

Table 4.6 Stiction variation from dithering applied to SJE in Panda arm with different frequency values.

Joint Configuration	*Base* τ_b *[Nm]*	τ_{SJE} *80 Hz [Nm]*	τ_{SJE} *50 Hz [Nm]*	τ_{SJE} *30 Hz [Nm]*	τ_{SJE} *15 Hz [Nm]*
Joint 1 Load (+)	0.5711	0.4741 (-16.98)	0.4467 (-21.79%)	0.4649 (-18.6%)	0.4601 (-19.45%)
Joint 1 Load (-)	-0.8287	-0.7389 (-10.84%)	-0.7017 (-15.32%)	-0.7832 (-5.49%)	-0.7185 (-13.3%)
Joint 1 No load (+)	0.85	0.8136 (-4.29%)	0.7412 (-12.8%)	0.7759 (-8.72%)	0.8356 (-1.7%)
Joint 1 No load (-)	-0.6501	-0.6774 (+4.19%)	-0.5953 (-8.43%)	-0.6471 (-0.47%)	-0.6693 (+2.95%)
Joint 2 Load (+)	1.079	0.8492 (-21.29%)	0.8784 (-18.59%)	0.8568 (-20.59%)	0.8086 (-25.06%)
Joint 2 Load (-)	-3.1321	-3.0586 (-2.35%)	-2.6186 (-16.39%)	-2.5781 (-17.69%)	-3.011 (-3.87%)
Joint 2 No load (+)	0.9935	0.97 (-2.36%)	0.9149 (-7.9%)	0.8702 (-12.41%)	0.9143 (-7.97%)
Joint 2 No load (-)	-0.9143	-0.8736 (-4.45%)	-0.8303 (-9.19%)	-0.7778 (-14.93%)	-0.8232 (-9.96%)
Joint 3 Load (+)	0.6549	0.5791 (-11.57%)	0.5932 (-9.42%)	0.5245 (-19.91%)	0.5943 (-9.25%)
Joint 3 Load (-)	-1.3366	-1.2893 (-3.54%)	-1.2271 (-8.19%)	-1.0698 (-19.96%)	-1.2487 (-6.58%)
Joint 3 No load (+)	0.7777	0.9042 (+16.27%)	0.8217 (+5.65%)	0.8045 (+3.45%)	0.8218 (+5.67%)
Joint 3 No load (-)	-0.6881	-0.5946 (-13.59%)	-0.5667 (-17.64%)	-0.5273 (-23.37%)	-0.5692 (-17.28%)
Joint 4 Load (+)	1.664	1.5418 (-7.35%)	1.4799 (-11.07%)	1.4942 (-10.2%)	1.6127 (-3.08%)
Joint 4 Load (-)	-0.5261	-0.4648 (-11.65%)	-0.4946 (-5.99%)	-0.492 (-6.5%)	-0.4876 (-7.32%)
Joint 4 No load (+)	1.2622	1.1354 (-10.05%)	1.1323 (-10.3%)	1.1462 (-9.19%)	1.1049 (-12.47%)
Joint 4 No load (-)	-0.5286	-0.4532 (-14.26%)	-0.4663 (-11.79%)	-0.4656 (-11.92%)	-0.4676 (-11.53%)
Joint 5 Load (+)	0.4707	0.4364 (-7.28%)	0.4355 (-7.48%)	0.4233 (-10.08%)	0.4082 (-13.28%)
Joint 5 Load (-)	-0.7224	-0.6499 (-10.04%)	-0.6383 (-11.63%)	-0.6399 (-11.42%)	-0.5531 (-23.43%)
Joint 5 No load (+)	0.5913	0.5652 (-4.42%)	0.5826 (-1.48%)	0.5792 (-2.06%)	0.5091 (-13.91%)
Joint 5 No load (-)	-0.506	-0.482 (-4.73%)	-0.4905 (-3.05%)	-0.496 (-1.96%)	-0.4567 (-9.74%)
Joint 6 Load (+)	0.4691	0.4576 (-2.45%)	0.4568 (-2.63%)	0.4637 (-1.17%)	0.444 (-5.35%)
Joint 6 Load (-)	-0.3941	-0.3821 (-3.04%)	-0.3779 (-4.12%)	-0.3805 (-3.44%)	-0.3656 (-7.24%)
Joint 6 No load (+)	0.3998	0.394 (-1.44%)	0.3901 (-2.42%)	0.3852 (-3.64%)	0.3823 (-4.37%)
Joint 6 No load (-)	-0.4878	-0.4839 (-0.79%)	-0.4664 (-4.37%)	-0.4728 (-3.06%)	-0.4619 (-5.3%)
Joint 7 Load (+)	0.6348	0.6101 (-3.89%)	0.6093 (-4.02%)	0.5684 (-10.46%)	0.3906 (-38.47%)
Joint 7 Load (-)	-0.6701	-0.689 (+2.82%)	-0.6682 (-0.28%)	-0.6212 (-7.29%)	-0.4298 (-35.85%)
Joint 7 No load (+)	0.604	0.5779 (-4.32%)	0.5667 (-6.18%)	0.5566 (-7.85%)	0.4294 (-28.92%)
Joint 7 No load (-)	-0.6314	-0.6071 (-3.85%)	-0.5855 (-7.27%)	-0.5569 (-11.8%)	-0.3907 (-38.13%)

After identifying the best frequencies for each joint, experiments were conducted to determine scale factors of the amplitudes that would further enhance the motion. Tables 4.7 and 4.8 show the application of scale factors of 1.2 and 0.8 to the *base* torque values τ_b, respectively, and the SJE was performed again with the same frequencies.

Table 4.7 Stiction variation from SJE for Panda with 1.2 scale factor applied to the *base* amplitudes.

Joint Configuration	τ_{SJE} *50 Hz (Nm)*	τ_{SJE} *30 Hz (Nm)*	τ_{SJE} *15 Hz (Nm)*
Joint 1 Load (+)	0.4426 (-22.51%)	0.4816 (-15.68%)	0.469 (-17.88%)
Joint 1 Load (-)	-0.7385 (-10.88%)	-0.7471 (-9.84%)	-0.7413 (-10.54%)
Joint 1 No load (+)	0.8214 (-3.36%)	0.7979 (-6.13%)	0.8804 (+3.57%)
Joint 1 No load (-)	-0.6926 (+6.53%)	-0.708 (+8.9%)	-0.7363 (+13.25%)
Joint 2 Load (+)	0.762 (-29.38%)	0.7258 (-32.74%)	0.8146 (-24.5%)
Joint 2 Load (-)	-2.6183 (-16.41%)	-0.1795 (-94.27%)	-2.9418 (-6.07%)
Joint 2 No load (+)	0.9177 (-7.63%)	0.8194 (-17.52%)	0.9676 (-2.6%)
Joint 2 No load (-)	-0.8448 (-7.6%)	-0.7999 (-12.51%)	-0.867 (-5.17%)
Joint 3 Load (+)	0.5592 (-14.62%)	0.5113 (-21.93%)	0.5557 (-15.14%)
Joint 3 Load (-)	-1.2038 (-9.93%)	-1.0449 (-21.82%)	-1.2796 (-4.27%)
Joint 3 No load (+)	0.8756 (+12.59%)	0.8815 (+13.34%)	0.8453 (+8.7%)
Joint 3 No load (-)	-0.5678 (-17.48%)	-0.5761 (-16.28%)	-0.5588 (-18.79%)
Joint 4 Load (+)	1.4195 (-14.7%)	1.4553 (-12.55%)	1.6098 (-3.26%)
Joint 4 Load (-)	-0.4648 (-11.66%)	-0.4747 (-9.78%)	-0.4691 (-10.84%)
Joint 4 No load (+)	1.1221 (-11.1%)	1.1443 (-9.34%)	1.0787 (-14.54%)
Joint 4 No load (-)	-0.4371 (-17.3%)	-0.4799 (-9.22%)	-0.4614 (-12.72%)
Joint 5 Load (+)	0.4256 (-9.57%)	0.4085 (-13.21%)	0.385 (-18.2%)
Joint 5 Load (-)	-0.6442 (-10.82%)	-0.6151 (-14.85%)	-0.5071 (-29.8%)
Joint 5 No load (+)	0.5884 (-0.5%)	0.5476 (-7.4%)	0.4624 (-21.8%)
Joint 5 No load (-)	-0.4972 (-1.74%)	-0.4809 (-4.96%)	-0.4254 (-15.93%)
Joint 6 Load (+)	0.4593 (-2.1%)	0.4495 (-4.18%)	0.4187 (-10.75%)
Joint 6 Load (-)	-0.3896 (-1.15%)	-0.3719 (-5.62%)	-0.3594 (-8.81%)
Joint 6 No load (+)	0.3777 (-5.52%)	0.3684 (-7.85%)	0.3646 (-8.82%)
Joint 6 No load (-)	-0.4724 (-3.15%)	-0.4614 (-5.4%)	-0.4471 (-8.35%)
Joint 7 Load (+)	0.5962 (-6.08%)	0.5386 (-15.16%)	0.3274 (-48.43%)
Joint 7 Load (-)	-0.6521 (-2.68%)	-0.5887 (-12.14%)	-0.3725 (-44.42%)
Joint 7 No load (+)	0.5603 (-7.23%)	0.527 (-12.76%)	0.3772 (-37.56%)
Joint 7 No load (-)	-0.5808 (-8.02%)	-0.523 (-17.17%)	-0.3198 (-49.36%)

Table 4.8 Stiction variation from SJE for Panda with 0.8 scale factor applied to the *base* amplitudes.

Joint Configuration	τ_{SJE} *50 Hz (Nm)*	τ_{SJE} *30 Hz (Nm)*
Joint 1 Load (+)	0.4843 (-15.21%)	0.4966 (-13.05%)
Joint 1 Load (-)	-0.7383 (-10.9%)	-0.7754 (-6.43%)
Joint 1 No load (+)	0.8288 (-2.49%)	0.8255 (-2.89%)
Joint 1 No load (-)	-0.7144 (+9.89%)	-0.7304 (+12.35%)
Joint 2 Load (+)	0.9335 (-13.48%)	0.8965 (-16.92%)
Joint 2 Load (-)	-2.7819 (-11.18%)	-2.7843 (-11.11%)
Joint 2 No load (+)	0.9767 (-1.69%)	0.9223 (-7.17%)
Joint 2 No load (-)	-0.849 (-7.14%)	-0.8423 (-7.88%)
Joint 3 Load (+)	0.5674 (-13.36%)	0.5502 (-15.99%)
Joint 3 Load (-)	-1.2626 (-5.53%)	-1.1976 (-10.4%)
Joint 3 No load (+)	0.9096 (+16.96%)	0.8963 (+15.25%)
Joint 3 No load (-)	-0.5859 (-14.85%)	-0.6039 (-12.23%)
Joint 4 Load (+)	1.5349 (-7.76%)	1.5375 (-7.61%)
Joint 4 Load (-)	-0.5186 (-1.44%)	-0.5006 (-4.85%)
Joint 4 No load (+)	1.1554 (-8.47%)	1.1639 (-7.79%)
Joint 4 No load (-)	-0.472 (-10.71%)	-0.4901 (-7.27%)
Joint 5 Load (+)	0.44 (-6.51%)	0.4322 (-8.17%)
Joint 5 Load (-)	-0.6275 (-13.13%)	-0.6357 (-12.01%)
Joint 5 No load (+)	0.5636 (-4.68%)	0.5772 (-2.39%)
Joint 5 No load (-)	-0.4824 (-4.65%)	-0.4945 (-2.27%)
Joint 6 Load (+)	0.4698 (+0.14%)	0.4606 (-1.83%)
Joint 6 Load (-)	-0.3818 (-3.11%)	-0.3794 (-3.72%)
Joint 6 No load (+)	0.3866 (-3.3%)	0.3899 (-2.48%)
Joint 6 No load (-)	-0.4759 (-2.43%)	-0.4743 (-2.77%)
Joint 7 Load (+)	0.6193 (-2.45%)	0.5962 (-6.08%)
Joint 7 Load (-)	-0.6725 (+0.36%)	-0.6407 (-4.39%)
Joint 7 No load (+)	0.5617 (-7.01%)	0.5533 (-8.4%)
Joint 7 No load (-)	-0.6106 (-3.3%)	-0.5825 (-7.75%)

Note that the 15 Hz frequency is absent from Table 4.8 since the results from the 0.8 scale factor were worse than those obtained from the 1.2 factor. Therefore, it was decided not to continue with that frequency value. However, for some joints of the Panda arm, the results from the 1.2 scale factor SJE were better than those without applying it.

After identifying both the frequencies and amplitudes, the dithering signals were constructed. The parameter selection was based on checking the feedback from the SJE, which involved identifying the conditions that decreased τ_{SJE} the most for each joint. Mixing these scale factors, which were applied to the *base* amplitudes, and frequencies for each of the joints, resulted in obtaining the so-called *intermediate* values or τ_i. However, the dithering signals produced in this section are intended to also be applied to the *Cartesian Impedance Controller* for trajectory experiments. Because the *intermediate* values are specific for load configuration and direction it was decided to simplify this and have only one value per joint.

Therefore, for each joint, the maximum absolute value from the four configurations of the *intermediate* values was selected and used as the dithering signal amplitude. The maximum absolute amplitudes from the *intermediate* values, along with the already assigned frequencies, were called *final* values or τ_F. Using these *final* values as the dithering parameters applied to the SJE produced the best results for the Panda arm. Table 4.9 shows the procedure for selecting these maximum absolute amplitudes. However, joint 2 was an exception since the maximum absolute amplitude was deemed too high (-3.7584 Nm) and was replaced by 1.2 Nm empirically. The results and improvements achieved from the *intermediate* and *final* values are presented in Table 4.10.

Figure 4.5 shows the robot response when sending a dithering signal using the *final* values. Note that the motion has reduced the stiction effect and reaches the threshold earlier than the one illustrated in Figure 4.3. The shaking effect in the joint motion produced by the dithering signal can also be seen.

Table 4.9 Choosing procedure and classification of the dithering signal parameters. (*) Joint 2 amplitude was an exception because of its high maximum absolute value.

Joint	Configuration	Frequency (Hz)	Scale Factor	*Base* τ_b (Nm)	*Intermediate* τ_i (Nm)	*Final* τ_F (Nm)
1	Load (+) Load (-) No Load (+) No Load (-)	50	1.0	0.5711 -0.8287 0.85 -0.6501	0.5711 -0.8287 0.85 -0.6501	0.85
2	Load (+) Load (-) No Load (+) No Load (-)	30	1.2	1.079 -3.132 0.9935 -0.9143	1.2948 -3.7584 1.1922 -1.0971	1.2 (*)
3	Load (+) Load (-) No Load (+) No Load (-)	30	1.0	0.6549 -1.337 0.7777 -0.6881	0.7859 -1.6044 0.9332 -0.8257	1.6044
4	Load (+) Load (-) No Load (+) No Load (-)	50	1.2	1.664 -0.5261 1.262 -0.5286	1.9968 -0.6313 1.5144 -0.6343	1.9968
5	Load (+) Load (-) No Load (+) No Load (-)	15	1.2	0.4707 -0.7224 0.5913 -0.506	0.5648 -0.8669 0.7096 -0.6072	0.8669
6	Load (+) Load (-) No Load (+) No Load (-)	15	1.2	0.4691 -0.3941 0.3998 -0.4878	0.5629 -0.4729 0.4798 -0.5854	0.5854
7	Load (+) Load (-) No Load (+) No Load (-)	15	1.2	0.6348 -0.6701 0.604 -0.6314	0.7618 -0.8041 0.7248 -0.7577	0.8041

Table 4.10 Stiction variation of SJE in Panda arm with *intermediate* and *final* amplitudes applied.

Joint Configuration	*Base* τ_b *(Nm)*	τ_{SJE} *Intermediate (Nm)*	τ_{SJE} *Final (Nm)*
Joint 1 Load (+)	0.5711	0.4514 (-20.96%)	0.4595 (-19.54%)
Joint 1 Load (-)	-0.8287	-0.7407 (-10.62%)	-0.7405 (-10.64%)
Joint 1 No load (+)	0.85	0.8418 (-0.96%)	0.7642 (-10.09%)
Joint 1 No load (-)	-0.6501	-0.7198 (+10.72%)	-0.6267 (-3.61%)
Joint 2 Load (+)	1.079	0.6576 (-39.05%)	0.7382 (-31.59%)
Joint 2 Load (-)	-3.1321	-3.1838 (+1.65%)	-3.0675 (-2.06%)
Joint 2 No load (+)	0.9935	0.8223 (-17.22%)	0.846 (-14.84%)
Joint 2 No load (-)	-0.9143	-0.8544 (-6.55%)	-0.8105 (-11.35%)
Joint 3 Load (+)	0.6549	0.525 (-19.84%)	0.3663 (-44.06%)
Joint 3 Load (-)	-1.3366	-1.1149 (-16.59%)	-1.0261 (-23.23%)
Joint 3 No load (+)	0.7777	0.8942 (+14.98%)	0.8648 (+11.2%)
Joint 3 No load (-)	-0.6881	-0.5958 (-13.41%)	-0.4233 (-38.49%)
Joint 4 Load (+)	1.664	1.4362 (-13.69%)	1.3958 (-16.12%)
Joint 4 Load (-)	-0.5261	-0.4782 (-9.12%)	-0.2961 (-43.72%)
Joint 4 No load (+)	1.2622	1.1434 (-9.41%)	1.0923 (-13.46%)
Joint 4 No load (-)	-0.5286	-0.4821 (-8.79%)	-0.4123 (-22%)
Joint 5 Load (+)	0.4707	0.377 (-19.89%)	0.2855 (-39.35%)
Joint 5 Load (-)	-0.7224	-0.5161 (-28.56%)	-0.516 (-28.57%)
Joint 5 No load (+)	0.5913	0.4559 (-22.9%)	0.4101 (-30.64%)
Joint 5 No load (-)	-0.506	-0.4213 (-16.73%)	-0.3286 (-35.06%)
Joint 6 Load (+)	0.4691	0.4266 (-9.07%)	0.4293 (-8.49%)
Joint 6 Load (-)	-0.3941	-0.3645 (-7.52%)	-0.3512 (-10.88%)
Joint 6 No load (+)	0.3998	0.3682 (-7.91%)	0.3667 (-8.28%)
Joint 6 No load (-)	-0.4878	-0.4488 (-7.99%)	-0.4566 (-6.38%)
Joint 7 Load (+)	0.6348	0.3252 (-48.77%)	0.3179 (-49.92%)
Joint 7 Load (-)	-0.6701	-0.3716 (-44.54%)	-0.3729 (-44.35%)
Joint 7 No load (+)	0.604	0.3768 (-37.62%)	0.3625 (-39.99%)
Joint 7 No load (-)	-0.6314	-0.32 (-49.31%)	-0.3121 (-50.57%)

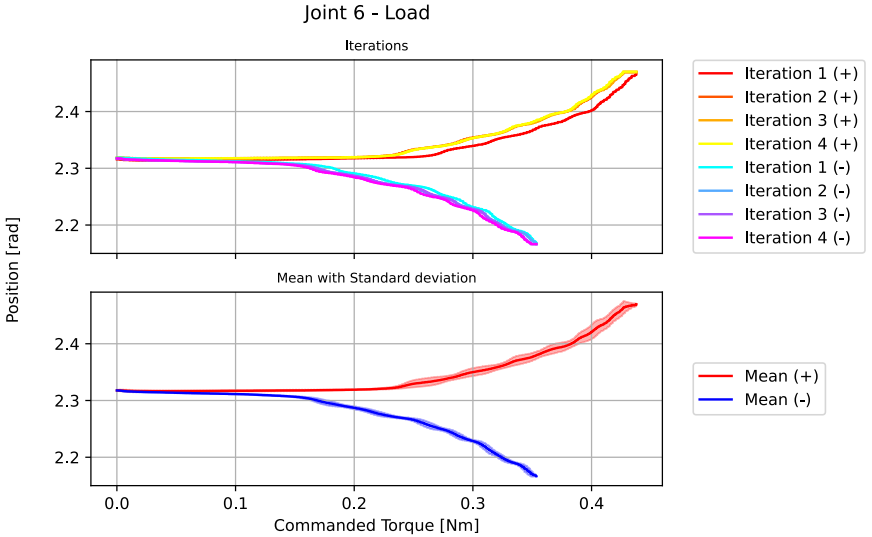

(a) Joint 6 Load configuration.

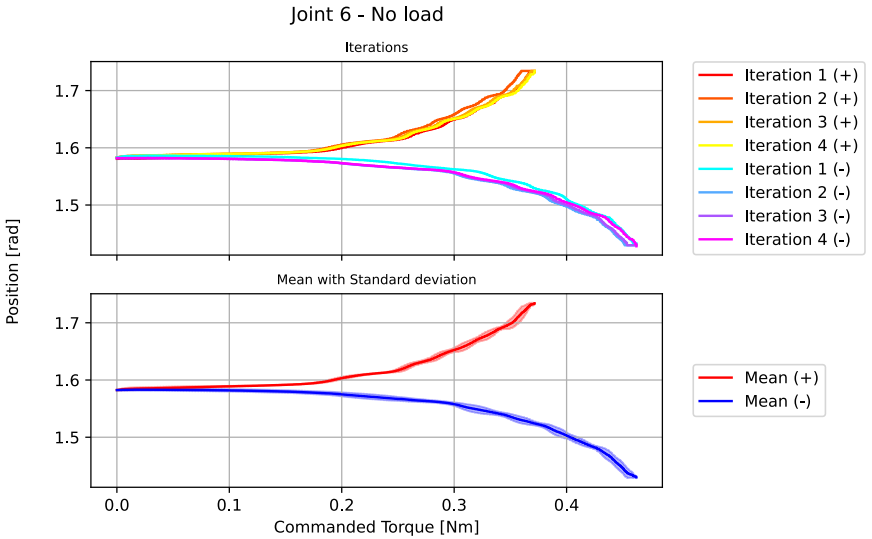

(b) Joint 6 No Load configuration.

Figure 4.5 Panda arm behaviour in SJE with *final* amplitudes and frequencies dithering applied. Note the vibrations in the end effector.

Generated Trajectory Experiment Improvement

The combinations of *final* amplitudes and frequencies for each joint of the Panda arm, described in Table 4.9, were implemented in the *Cartesian Impedance Controller* and their impact on the system's behavior was evaluated by testing them on selected trajectories. Specifically, the dithering signals were applied as the controller was following some trajectory points describing a triangle shape in 3D space and a pentagon in the XY-plane.

The trajectory experiments were conducted with different Cartesian stiffness values of 200 N/m translational stiffness and 20 N/m rotational stiffness, as well as 400 N/m translational and 40 N/m rotational stiffness. The nullspace stiffness was always set to 0 N/m. All the experiments were done in 10 iterations to ensure that the results were consistent and reliable. Conducting the experiments multiple times also allowed for the calculation of mean error and standard deviation, which provided a quantitative measure of the performance.

The results of the experiments can be seen in Figure 4.6, which show the trajectories followed by the Panda arm end effector with and without the dithering signal applied to the controller, plotted together with the reference. It can be appreciated how the dithered trajectory approximates to the reference better than the non-dithered one, especially when arriving or moving from a point. The higher stiffness case, shown in Figures 4.6b and 4.6d, illustrates how both dithered and non-dithered trajectories follow the reference better than the low stiffness ones, illustrated in Figures 4.6a and 4.6c. The stiffness values shown in Figure 4.6 captions are ordered as translational, rotational and nullspace, respectively. The 3D plots for the triangle and pentagon trajectories with different stiffness values, where the Z coordinate is also represented, can be found in Appendix E.

The impact of dithering on position and orientation errors was evaluated by comparing the non-dithered trajectories with the dithered ones, and the results are presented in Figures 4.7 and 4.8. The comparison is shown for the X, Y and Z coordinates separately, while the orientation errors (roll, pitch, and yaw) are included in Appendix F. The differentiation between stiffness scenarios reveals that dithering has a more pronounced impact in the higher stiffness case, generally reducing the error but in exchange of increasing the standard deviation in the experiments.

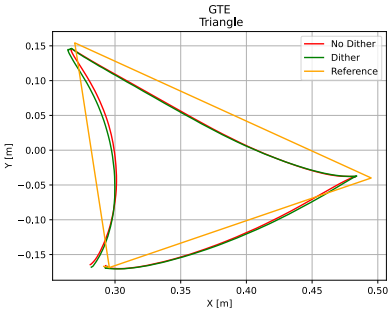

(a) Triangle with 200/20/0 stiffness.

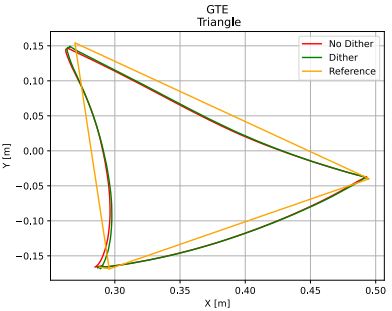

(b) Triangle with 400/40/0 stiffness.

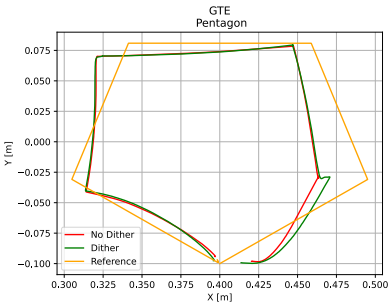

(c) Pentagon with 200/20/0 stiffness.

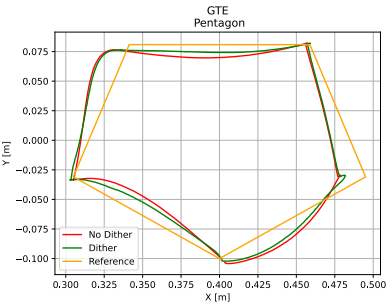

(d) Pentagon with 400/40/0 stiffness.

Figure 4.6 Triangle and pentagon 2D trajectory results from the GTE. The dithering case follows the trajectory better than the non-dithering one.

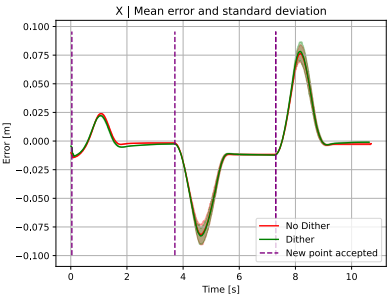

(a) X coordinate, 200/20/0.

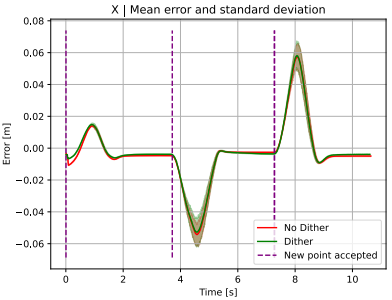

(b) X coordinate, 400/40/0.

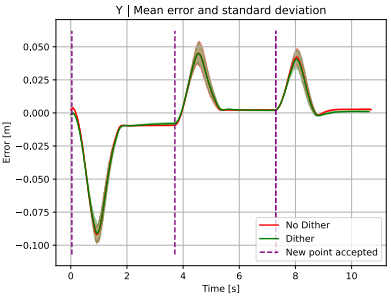

(c) Y coordinate, 200/20/0.

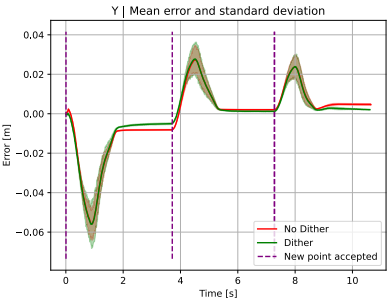

(d) Y coordinate, 400/40/0.

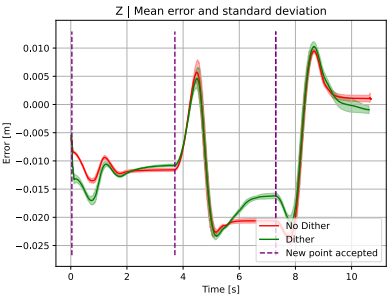

(e) Z coordinate, 200/20/0.

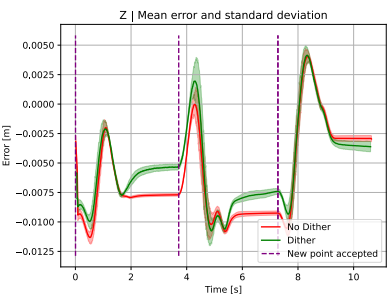

(f) Z coordinate, 400/40/0.

Figure 4.7 Mean error and standard deviation results for the triangle trajectory from the GTE.

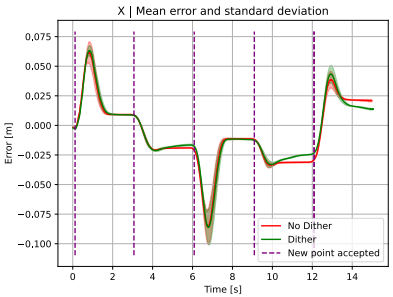

(a) X coordinate, 200/20/0 stiffness.

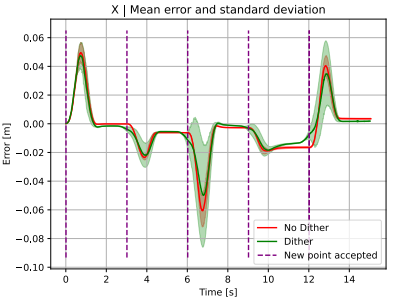

(b) X coordinate, 400/40/0 stiffness.

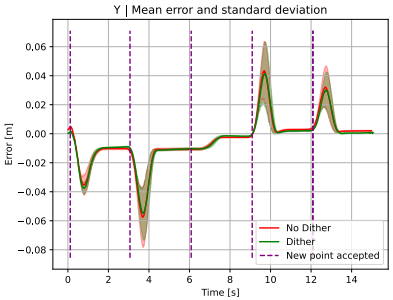

(c) Y coordinate, 200/20/0.

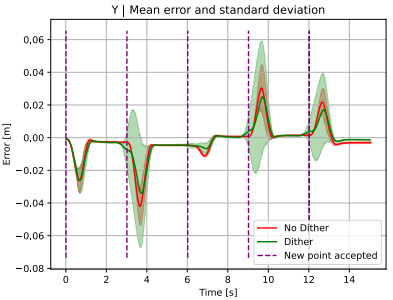

(d) Y coordinate, 400/40/0.

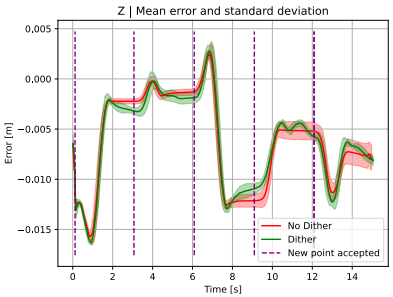

(e) Z coordinate, 200/20/0.

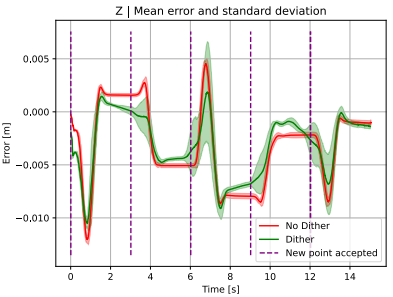

(f) Z coordinate, 400/40/0.

Figure 4.8 Mean error and standard deviation results for the pentagon trajectory from the GTE.

Table 4.11 shows the tables of the mean error quantitative comparisons between the dither and non-dither case. Mean errors in absolute terms were calculated by summing the error values for each coordinate within a specified time window. The time window extended from 1 second before the last accepted new point to 1 second after the last accepted new point, which because of the sampling period resulted in 200 data points. Since the end effector was arriving and moving from a point, the robot worked under low-speed regimes, where stiction generally appears. It can be seen that the mean error differences are mostly negative, which means the mean errors are reduced when applying dithering.

Table 4.11 Quantitative mean error comparison for each axis in the different trajectories around the last point. The differences between mean errors are mostly negative.

Axis	Dither (Nm)	No Dither (Nm)	Diff. (Nm)
x	4,9767	4,7874	+0,1893
y	2,5496	2,6343	-0,0847
z	3,3246	4,0389	-0,7143
roll	2,1881	3,3252	-1,1371
pitch	9,2094	10,6012	-1,3918
yaw	4,6985	5,2760	-0,5775

(a) Triangle 200/20/0

Axis	Dither (Nm)	No Dither (Nm)	Diff. (Nm)
x	3,5112	3,4076	+0,1037
y	1,5975	1,7436	-0,1461
z	1,3487	1,5816	-0,2329
roll	0,9408	1,8383	-0,8976
pitch	3,1052	3,8111	-0,7059
yaw	3,4507	3,5692	-0,1185

(b) Triangle 400/40/0

Axis	Dither (Nm)	No Dither (Nm)	Diff. (Nm)
x	5,0474	5,5658	-0,5184
y	2,0089	2,2624	-0,2535
z	1,3682	1,3053	+0,0629
roll	1,1683	0,5344	+0,6339
pitch	9,2910	10,8895	-1,5986
yaw	3,6577	4,8327	-1,1751

(c) Pentagon 200/20/0

Axis	Dither (Nm)	No Dither (Nm)	Diff. (Nm)
x	3,0126	3,8932	-0,8806
y	1,1852	1,3040	-0,1188
z	0,6746	0,7088	-0,0343
roll	1,1286	0,3993	+0,7292
pitch	4,3424	6,5154	-2,1730
yaw	2,0837	2,7623	-0,6786

(d) Pentagon 400/40/0

5

Discussion

This chapter discusses the project's procedures and obtained results.

5.1 Stiction Characterization

Several issues were encountered during trajectory generation with `RosDyn`. A significant challenge was found when generating trajectories as the majority of the trajectories did not work on the actual robot because of various reasons. One of the issues observed was that the generated trajectories were not continuous, causing the reference pose to skip certain intermediate poses and jump abruptly from one point to another. This behavior indicated that there was a problem with the generated trajectory and that the end effector would not follow the reference pose precisely. Different approaches were attempted to fix or reduce the occurrence of this issue, including reducing the duration of the trajectory, decreasing the maximum step between points, and using alternative motion planning algorithms. After trying these methods, the problem was resolved to some extent, and a few jump-free trajectories were obtained.

Another problem was related to the difference in collision detection between `RosDyn` (`MoveIt!`) and the internal controller of the Panda robot that handles safety. The collision detection of the Panda internal controller was found to be stricter than `MoveIt!`'s, causing the internal controller to stop the robot due to collision detection when the generated trajectories were executed on the robot. To address this issue, `MoveIt!`'s collision detection was increased to better match the internal controller, but the problem persisted. It was then discovered that collision detection occurred only when one of the joints was approaching a specific position threshold. The solution was to change that joint limit in the `MoveIt!` configuration file, which solved the problem.

Furthermore, a bug was encountered in the code when `RosDyn` attempted to estimate the model, where it would not be able to complete the estimation. With the

help of a supervisor, the bug was eventually fixed, and `RosDyn` could proceed with the estimation process. However, the results were not reasonable, as can be seen in Table 4.1, and therefore an alternative approach was explored. The idea was to estimate the model using the values provided in the `libfranka` library with the generated trajectories. However, the results were again mostly unexpected, with only joint 7 showing expected results. Investigation through the data revealed that the acceleration was quite noisy, and an exponential smoothing filter was applied to it. However, the results did not improve significantly. Despite further investigation and attempted fixes, the cause of the unreasonable results could not be determined, and the approach was abandoned.

A comparison between the LSM and the SJE stiction characterization is stated in Table 4.4. Looking at the friction-velocity plots presented in Appendix A, it was already expected to have unreasonable results from the LSM, since the plots did not look similar to Figure 2.3 or the one obtained for joint 7 represented in Figure 4.1a. It was initially suspected that the problem relied on the trajectory used to obtain the friction-velocity data sets, but every trajectory produced unreasonable results. Another hypothesis is that the problem may be because of the gravity terms extracted from `libfranka` since the friction torque values calculated reached values up to 15 Nm in absolute terms. It was also thought that the issue could come from having speed regimes out of the stiction region, but even after reducing the velocity in the trajectories, the results obtained were still unacceptable.

To obtain the base values for the dithering amplitudes, the Single Joint Experiment (SJE) was used instead. The SJE determined the minimum stiction torque values required to move until the joint reached a particular position threshold from a specific configuration and was deemed suitable for obtaining the base values. Moreover, SJE was simpler to execute since it did not require third-party software or complex calculations, and the experiment could be conducted on any torque-based robot with a torque controller.

A limitation of the SJE is that the acquired torques correspond to a specific joint configuration and rotational direction. Nonetheless, there exist techniques to obtain generalized values from the acquired torques for each of the joints. One approach is to compute the average torques for the *Load* and *No Load* configurations, and then determine the midpoint of the positive and negative values as an offset, which is subsequently added to the dithering signal. This technique is independent of direction and load. Another strategy involves selecting the largest magnitude torque value for each joint to ensure that the torque exceeds the stiction, regardless of the load or direction. This was found to produce favorable results. However, it is crucial to note that SJE solely applies to a specific joint configuration, and the obtained values might not be sufficient for another joint configuration even if they are under a similar load. To address this issue, various scaling factors of the dithering ampli-

tudes were experimented with, yielding moderate success.

A phenomenon was observed during the SJE application. It happened in both dithering and non-dithering scenarios for every joint. It can be observed in Figures 4.2, 4.3, and 4.4, where the first iteration behaves differently from the rest. It may start to move and reach the threshold before the others, as can be seen in Figure 4.2b, or just the opposite, as illustrated in Figure 4.3a. This phenomenon probably occurs because of the motion of the joint motor, which behaves differently when switching from one rotation direction to another. Since the robot moves back to a reset pose, the next first iteration needs to switch rotational direction.

5.2 Dithering Results

As has been explained, dithering was applied to both SJE and GTE. Improvements in robot motion were more noticeable in the first case, even though the results were promising in both experiments.

The chosen dithering frequencies used to improve the SJE in both robot arms were initially merely arbitrary. The idea was to find an approximate frequency range that would improve the robot's motion through dithering and discard those that did not, as happened with the frequency value of 80 Hz in the Panda arm. Following the same reasoning, the scale factors of 1.2 and 0.8 were applied, although it was decided not to increase the amplitudes more than 1.2 to prevent the robot from vibrating too much. The vibrations observed in the robot when applying dithering with the *final* values in the experiments were subtle. They could hardly be seen by eye but could be heard in some poses, as well as noticeably felt when touching the robot. The number of iterations for the SJE was initially set at 6, but was later reduced to 4 when working with the Panda arm to save time shortening the experiments.

Comparisons of Figure 4.3a with Figure 4.3b reveal that the stiction is mitigated for both load and no load configurations as the robot's motion becomes smoother and the threshold is reached earlier. As illustrated in Table 4.10, the torque needed to reach the threshold (τ_{SJE}) is reduced between approximately 6 and 10% from the *base* case (τ_b) for joint 6 of the Panda arm. It is worth noting that joint 6 exhibits a lower torque reduction compared to, for example, joints 5 and 7, which have reductions of up to 50% in τ_{SJE} when applying dithering using the *final* parameters. Appendices C and D contain the plots for each configuration and joint without and with dithering, respectively, so they can be compared to see the experiment upgrade. In the plots that include the dithering signals applied, it can be observed how dithering creates a shaking effect in the robot joints' motion, which must be regulated so the trajectories and the robot arm integrity are not affected by it.

The triangle and pentagon plots shown in Figure 4.6 represent the mean of 10 iteration trajectories described by the end effector for both dithering and non-dithering scenarios, as well as the reference. Qualitatively, it can be seen that the dithered trajectories follow the reference closer than the non-dithered ones. This already shows that the results obtained are encouraging. It is also important to contrast how stiffness affects these experiments, where the trajectories in Figures 4.6b and 4.6d are closer to the reference than the ones in Figures 4.6a and 4.6c.

Figures 4.7 and 4.8 show the mean error and standard deviation for each Cartesian coordinate of the trajectories shown in Figure 4.6. The same GTE but with different stiffness values are compared left and right, coordinate by coordinate (X, Y, and Z). Even though the whole trajectory must be analyzed, the most interesting points of the plots for this thesis are those where the velocity is close to zero since stiction is present. These points are basically the regions close to the moments where the controller is accepting a new goal, indicated by a purple vertical dotted line. The ideal solution in this experiment would be a zero error and standard deviation; therefore, the closer the trajectory errors are to these values, the better. Even though in some cases the mean error is increased (in absolute terms), generally the dithered trajectories reduce the mean error. This effect is more noticeable in the case of higher stiffness, especially in Figures 4.8f and 4.7f. However, it can also be observed how the standard deviation increases with the stiffness, probably because of to the shaking effect in the robot joints. Summarizing, the dithering impact is more noticeable for higher values of stiffness, originating in a trade-off between a general decrease of the mean error and an increase in the standard deviation.

As a general comparison between the experiments, the improvements for the SJE were greater than those for the GTE. Under ideal circumstances, as the ones recreated in the SJE environment, with low-speed regimes from a static position and a specific dithering signal prepared for every joint, the stiction, error, and standard deviation in the experiment are reduced with almost no drawbacks. Nevertheless, when the dithering signals extracted from the SJE are generalized and applied to the various joints together, the results are no longer that pronounced. The fact that the GTE involves movements and velocities that are not as ideal as the ones prepared for the SJE, has to be taken into account even though the triangle and pentagon trajectories were thought to be as close as possible to the ideal stiction circumstances of the SJE. One way to improve the GTE could be to adapt the dithering signal amplitudes to a function of velocity, so that the dithering impact is reduced when the low-speed regimes disappear.

6

Conclusions

As stated in the problem formulation of this thesis, the first objective was to identify and characterize stiction in the joints of robot arms. The second objective was to apply dithering to mitigate its effects, resulting in improved motion accuracy of the robot arms when using Cartesian impedance control. The results of this thesis indicate that the objective has been achieved, as the application of dithering has reduced stiction and improved the accuracy of the robot, as demonstrated by a reduction in trajectory errors of the robot end effector.

Despite encountering various difficulties during the identification and modeling procedures, alternative methods of characterizing stiction were identified and developed, namely the Single Joint Experiment (SJE), providing an empirical procedure that can be applied to torque-controlled robot arms.

Determining the stiction band values for the robot is a critical step in ensuring that the dithering signals effectively mitigate stiction. However, obtaining these values through dynamics identification may be challenging, depending on the type of robot arm. Thus, experiments such as the Single Joint Experiment (SJE) can serve as a useful starting point, as evidenced by the results. The SJE results indicated a significant improvement in torque reduction. Nonetheless, these improvements were only marginal in the Generated Trajectory Experiment (GTE), suggesting that further adjustments to the dithering signals could have been made. Still, the results from the GTE are promising, showing that dithering is a complex but useful technique to take into account.

6.1 Future Work

Although the thesis has made significant progress in characterizing stiction and improving the robot's motion using dithering, there are still several avenues for future work:

- To look for a more complex model of stiction, not summarizing it into stiction bands with a positive and negative value but as a part of a friction model that includes every friction component as well as the Stribeck's effect also.
- To explore a more efficient and reliable method of obtaining parameters for the dithering signal. This could help streamlining the process when implementing dithering on different robots.
- To investigate the possibility of turning dithering on/off depending on whether it is needed or not. One idea is to have the amplitude of the dithering signal be a function of the velocity, which could help in the use of the dithering signal.
- To experiment with different types of dithering signals instead of a sinusoidal wave. For example, a rectangular function or a specialized signal for trajectories, to determine whether they could further improve the performance of the robot.
- To completely remove the shaking effect from the end effector by better adapting dithering to trajectory experiments so it does not affect the robot's accuracy.
- To conduct studies about the energy efficiency of dithering when applied to the robot, as well as to investigate how it affects the joint motor gears.

A

Appendix — Friction-Velocity Results for Panda Arm Joints

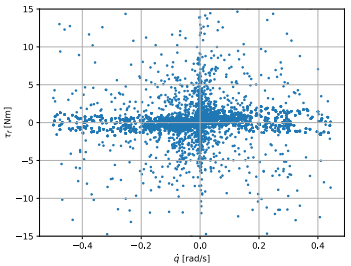

(a) Joint 1.

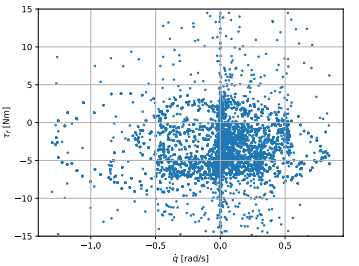

(b) Joint 2.

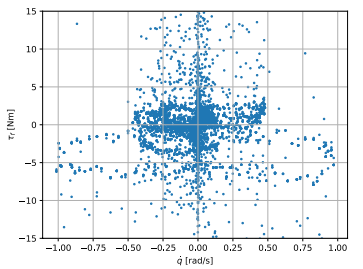

(c) Joint 3.

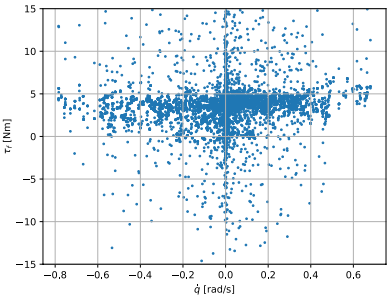

(d) Joint 4.

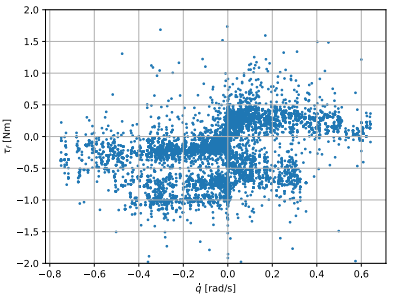

(e) Joint 5.

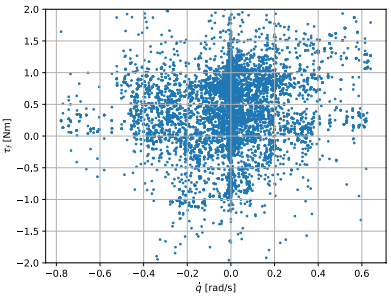

(f) Joint 6.

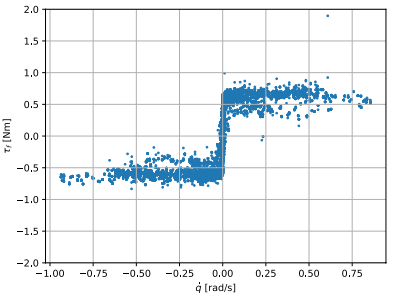

(g) Joint 7.

Figure A.1 Friction-velocity plots from LSM for Panda arm joints.

Table A.1 LSM estimation values for the Panda arm joints.

Joint	*Intercept*	*Slope*	R^2
Joint 1 (+)	0.8138	-3.0215	0.002346
Joint 1 (-)	-0.2150	0.0440	0.000001
Joint 2 (+)	-3.1325	0.4349	0.000233
Joint 2 (-)	-4.1755	-0.6798	0.000549
Joint 3 (+)	1.0559	-5.2426	0.010441
Joint 3 (-)	0.1632	3.9886	0.017101
Joint 4 (+)	3.4506	2.7081	0.002740
Joint 4 (-)	2.7097	-1.4257	0.001891
Joint 5 (+)	-0.0394	0.2712	0.005125
Joint 5 (-)	-0.3908	0.0692	0.000666
Joint 6 (+)	0.3740	0.7220	0.016532
Joint 6 (-)	0.3907	0.1552	0.000767
Joint 7 (+)	0.5576	0.1209	0.029948
Joint 7 (-)	-0.5395	0.1198	0.041832

B

Appendix — Single Joint Experiment Plots for LBR iiwa Arm

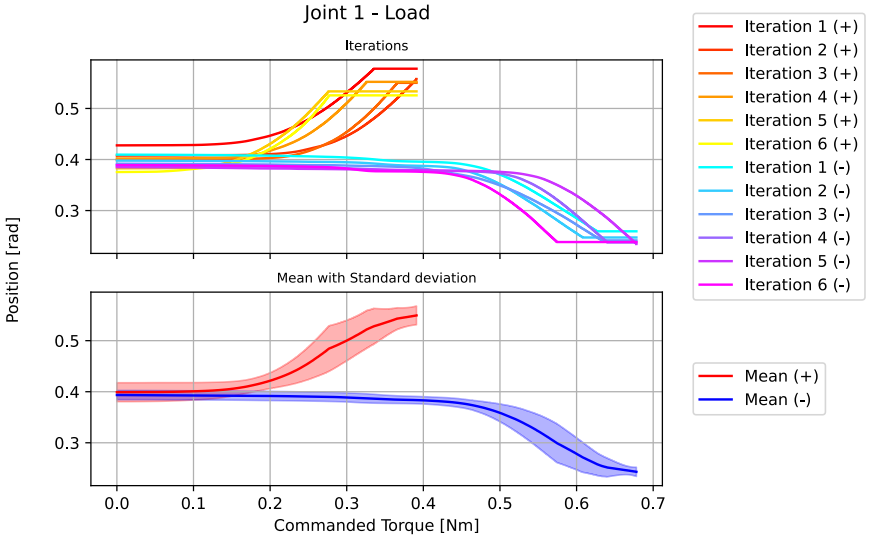

(a) Load configuration.

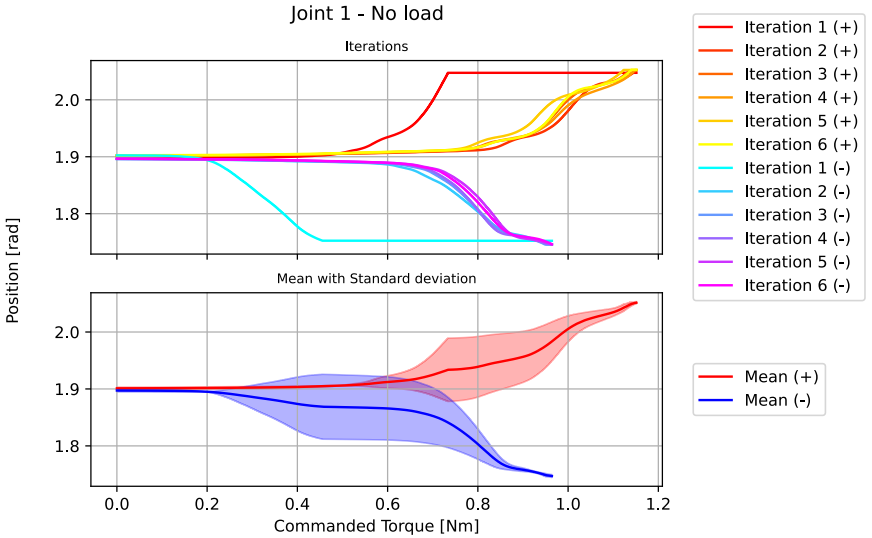

(b) No Load configuration.

Figure B.1 SJE in LBR iiwa joint 1 without dithering.

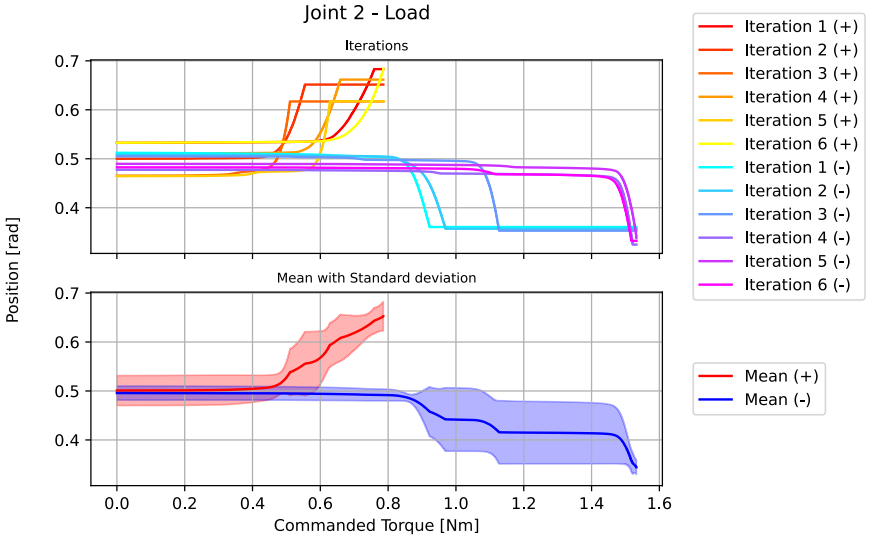

(a) Load configuration.

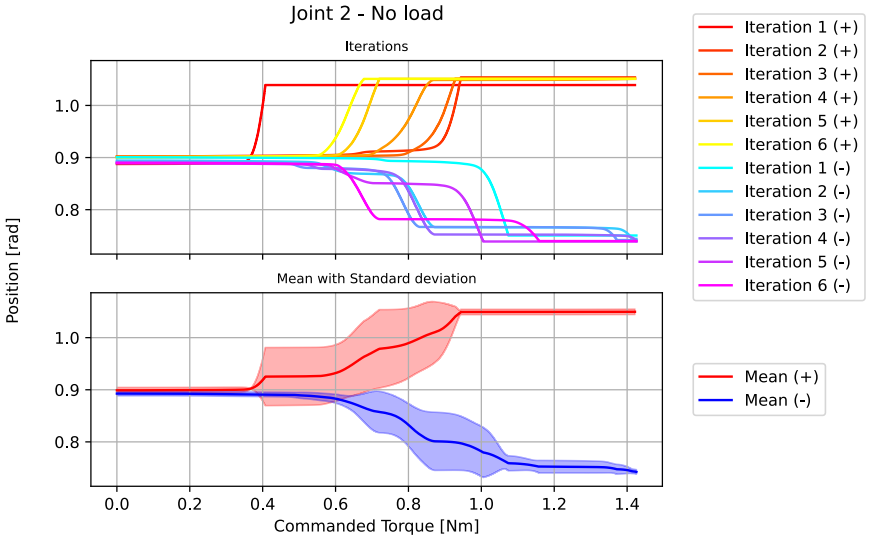

(b) No Load configuration.

Figure B.2 SJE in LBR iiwa joint 2 without dithering.

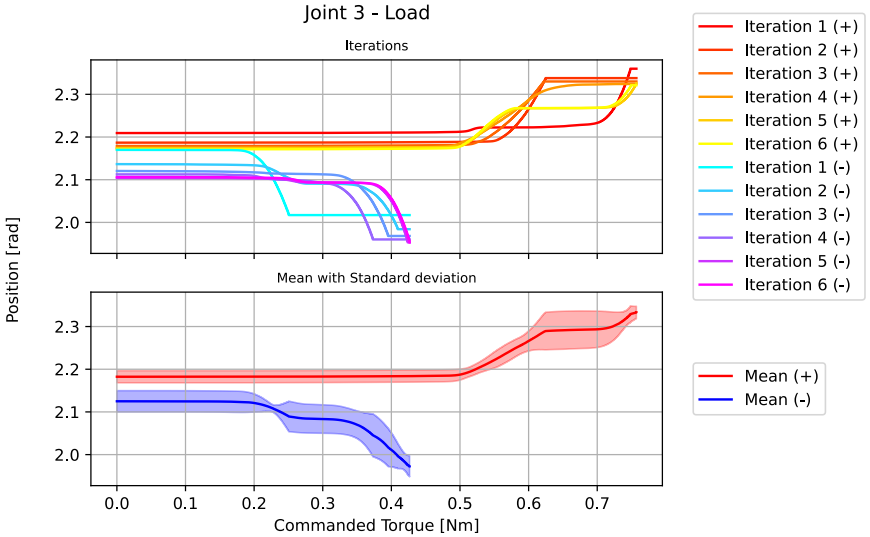

(a) Load configuration.

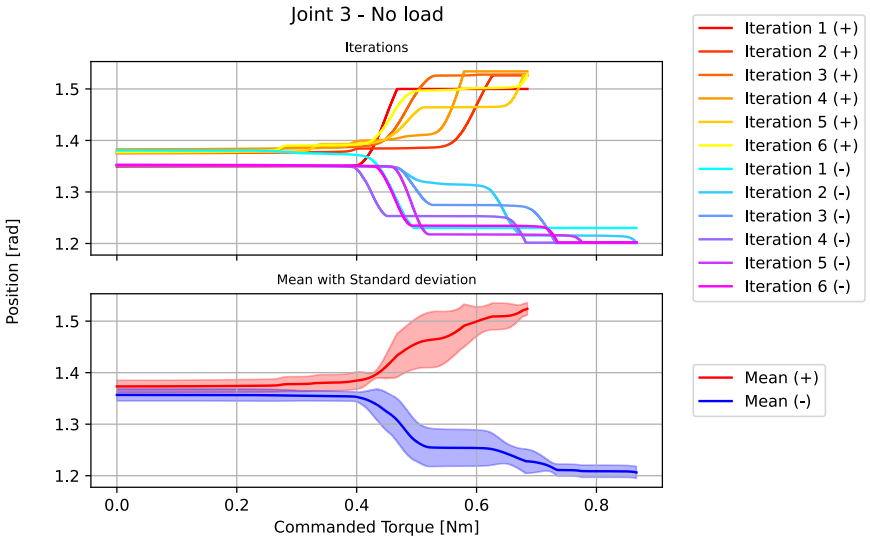

(b) No Load configuration.

Figure B.3 SJE in LBR iiwa joint 3 without dithering.

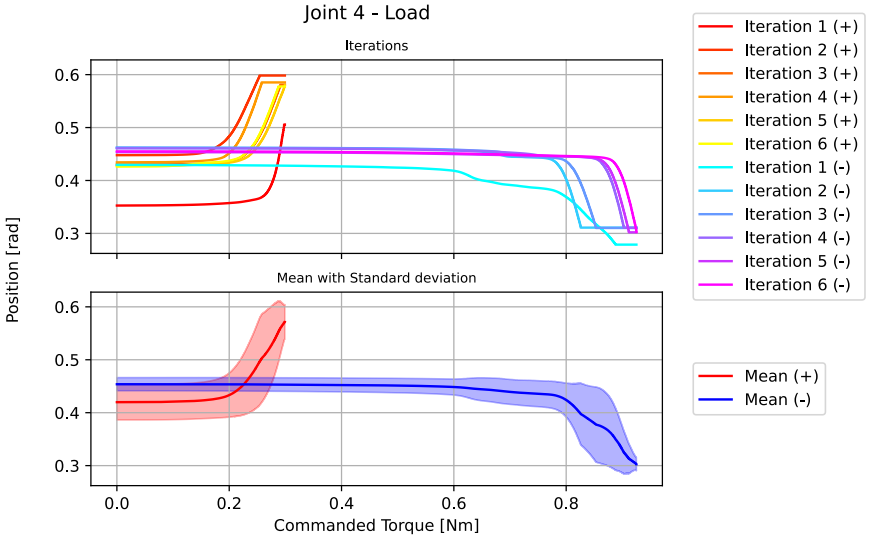

(a) Load configuration.

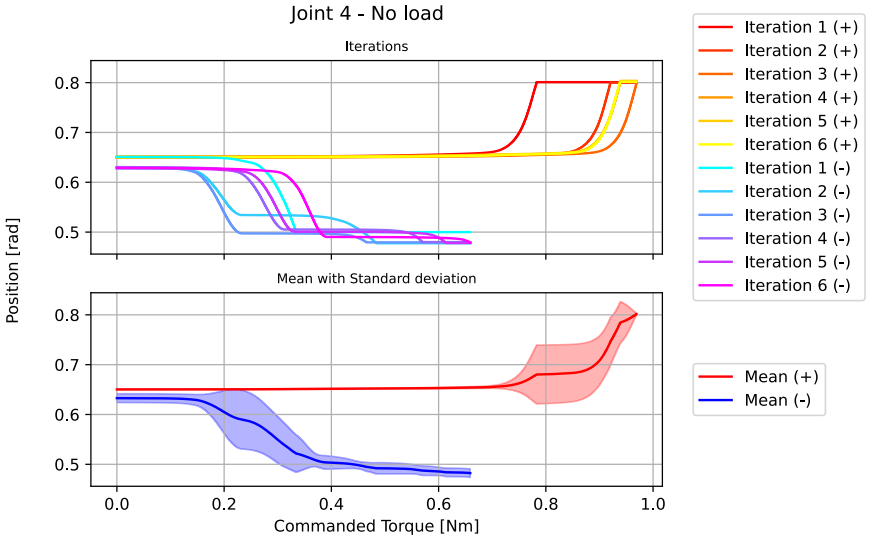

(b) No Load configuration.

Figure B.4 SJE in LBR iiwa joint 4 without dithering.

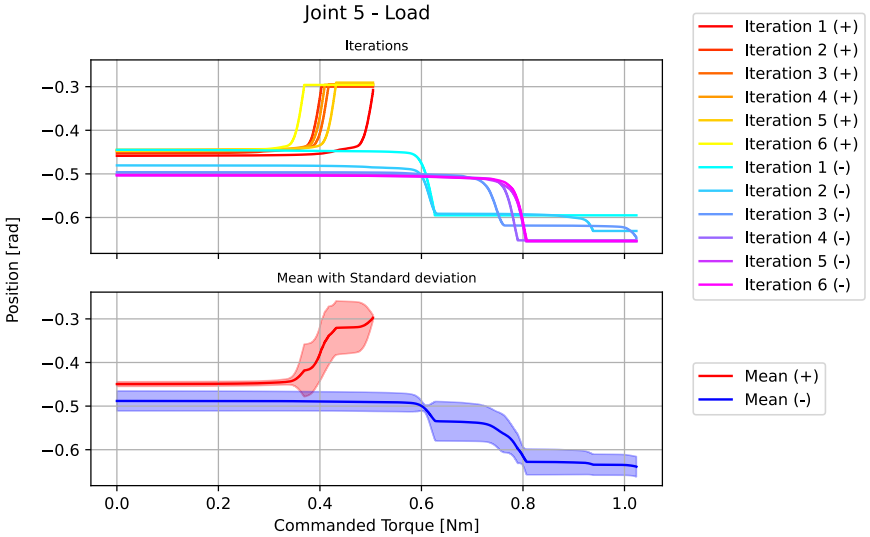

(a) Load configuration.

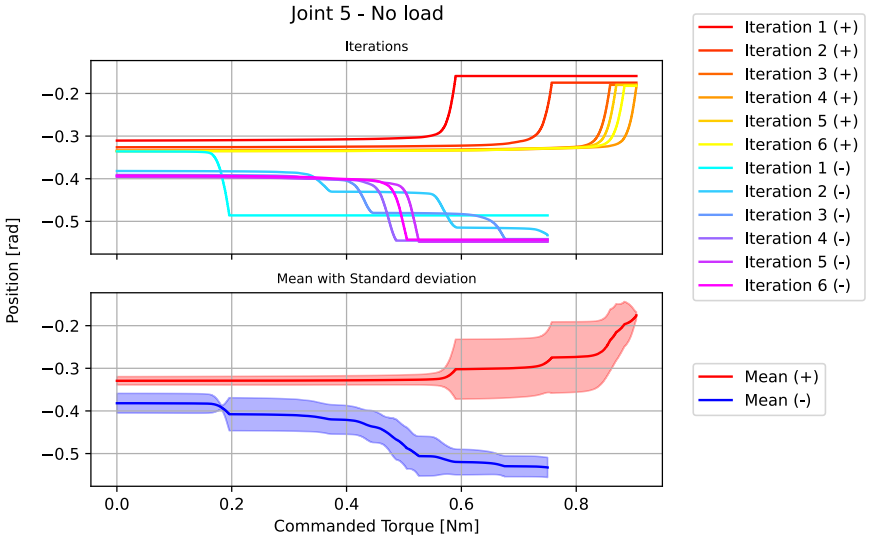

(b) No Load configuration.

Figure B.5 SJE in LBR iiwa joint 5 without dithering.

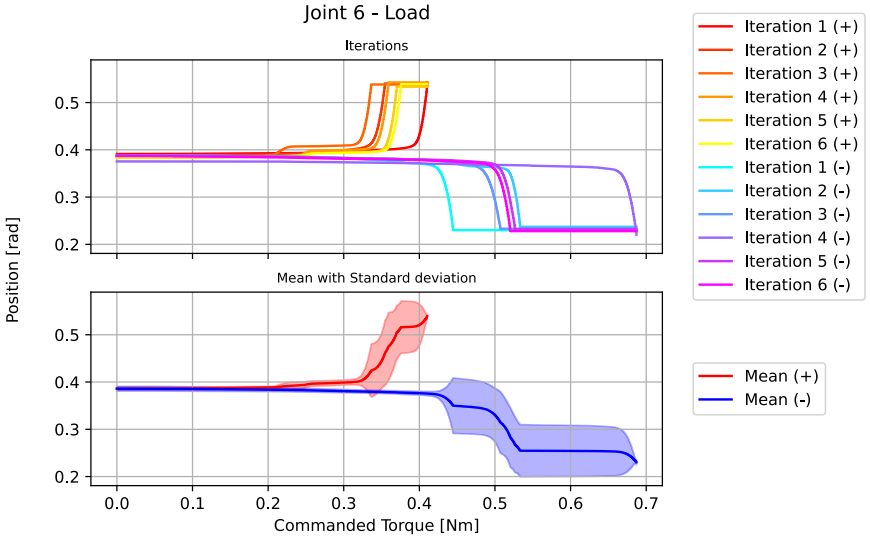

(a) Load configuration.

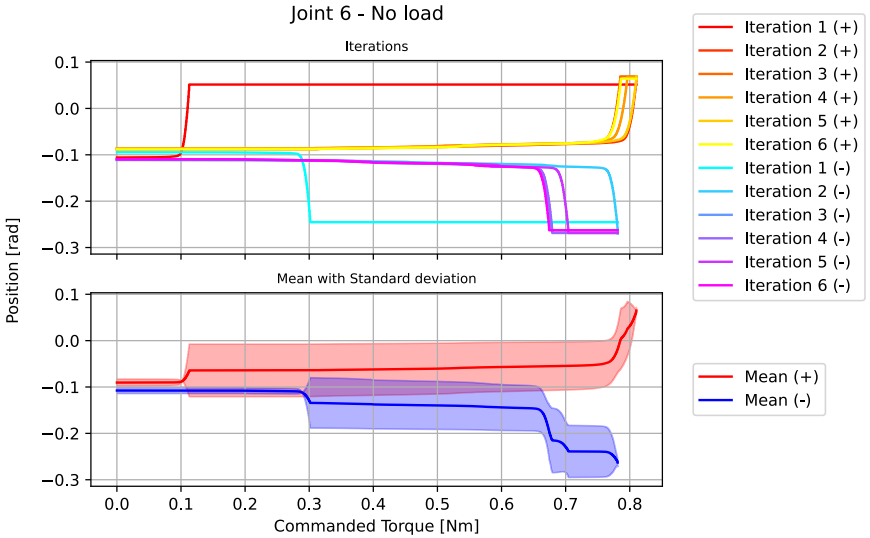

(b) No Load configuration.

Figure B.6 SJE in LBR iiwa joint 6 without dithering.

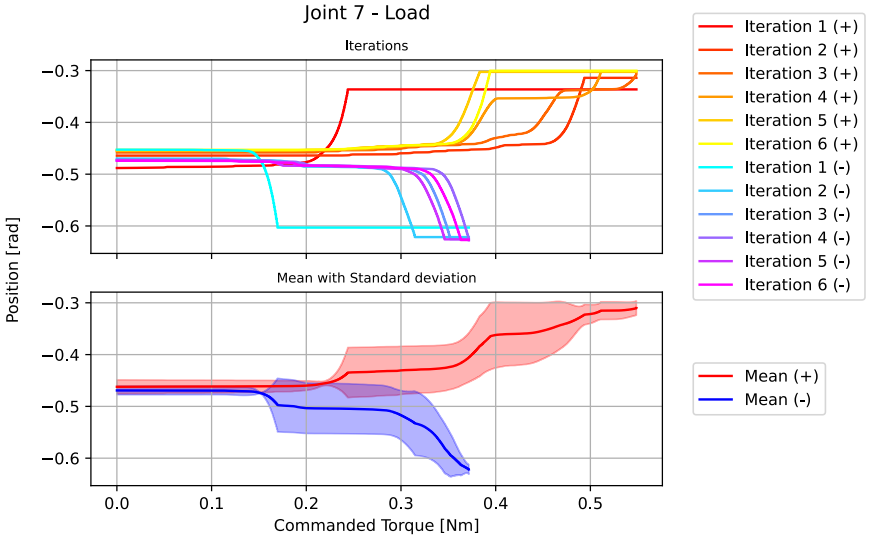

(a) Load configuration.

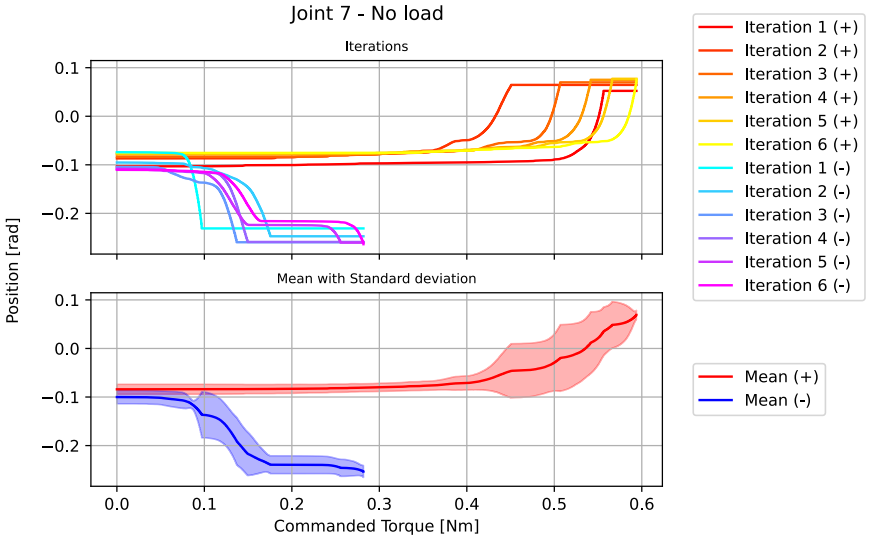

(b) No Load configuration.

Figure B.7 SJE in LBR iiwa joint 7 without dithering.

C

Appendix — Single Joint Experiment Plots for Panda Arm

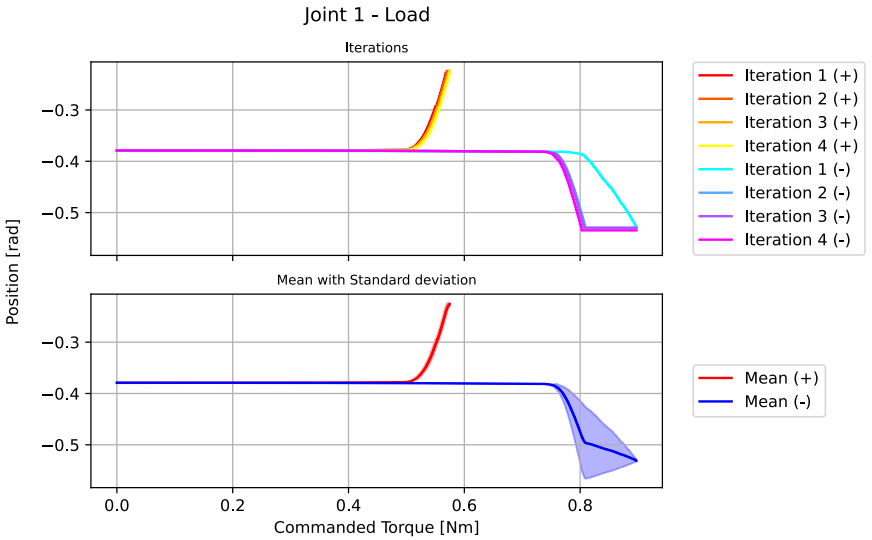

(a) Load configuration.

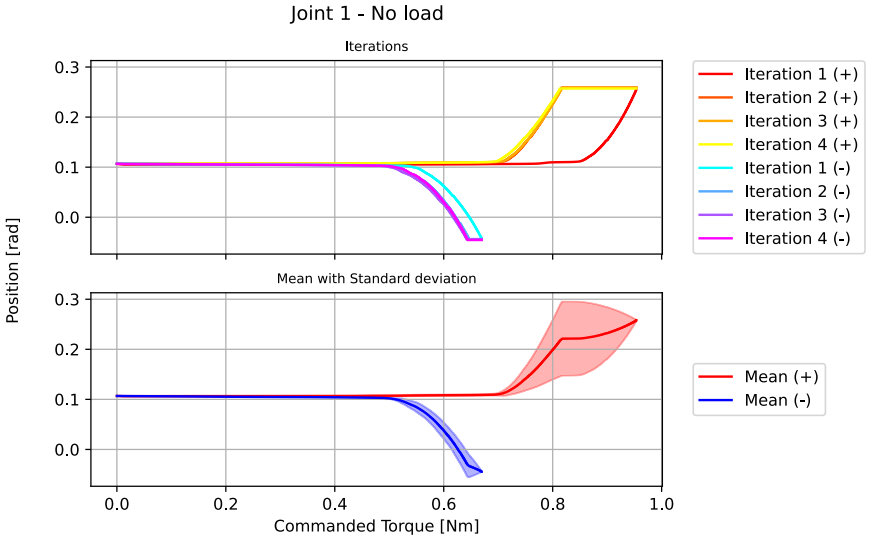

(b) No Load configuration.

Figure C.1 SJE in Panda arm joint 1 without dithering.

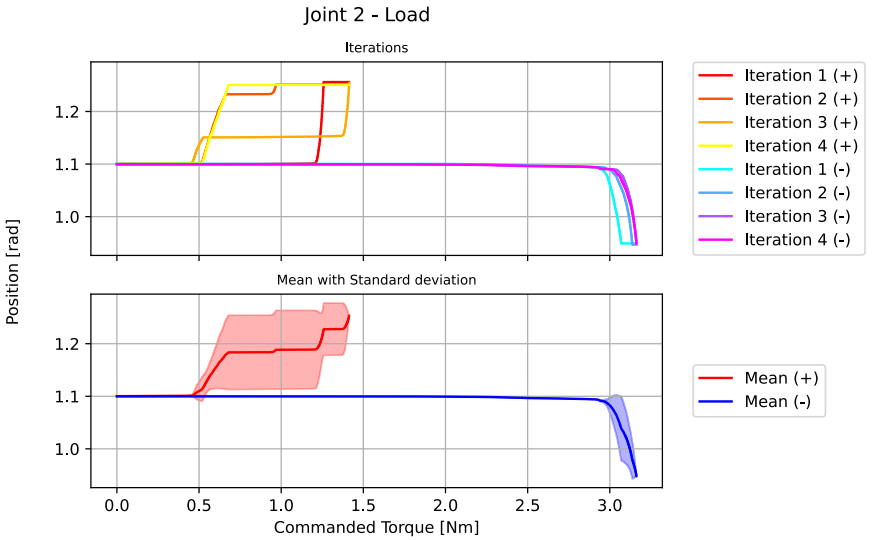

(a) Load configuration.

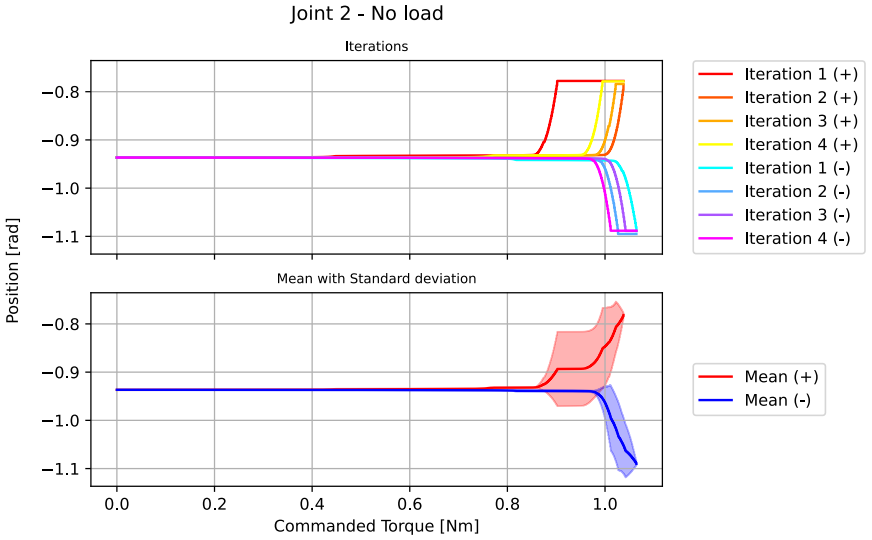

(b) No Load configuration.

Figure C.2 SJE in Panda arm joint 2 without dithering.

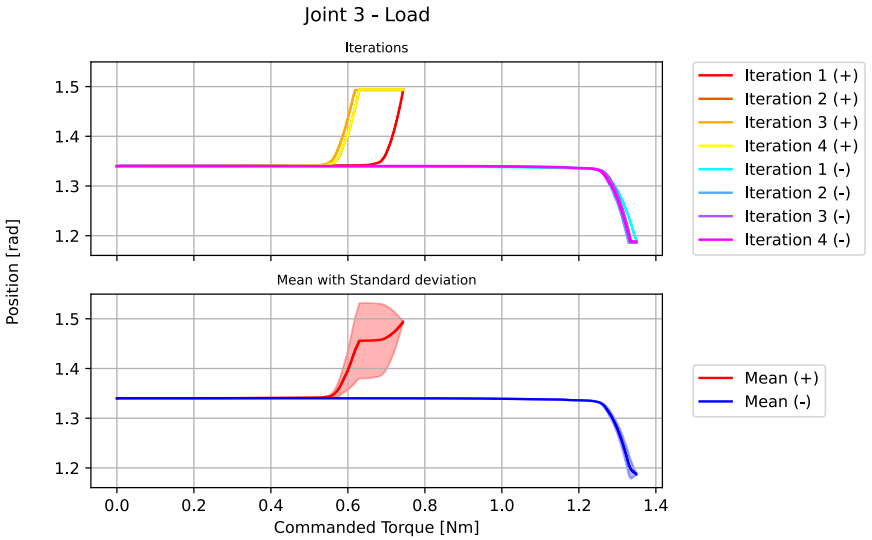

(a) Load configuration.

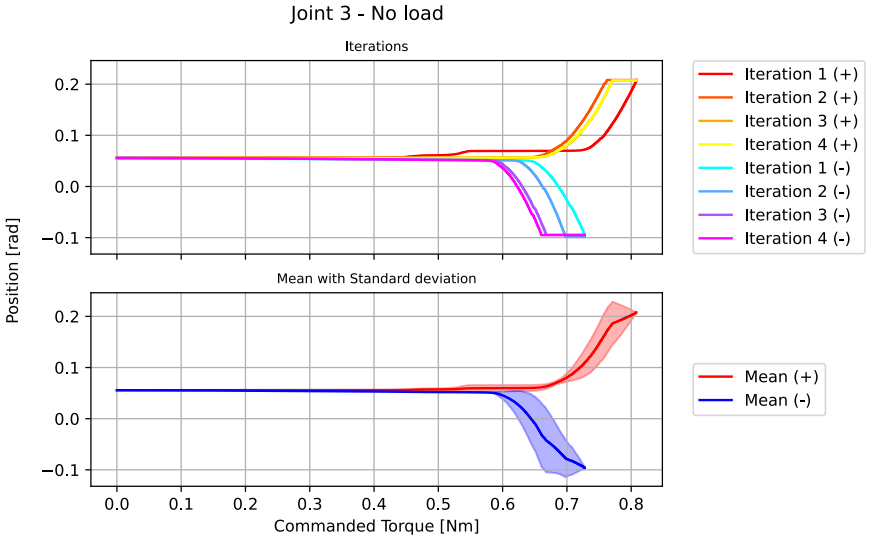

(b) No Load configuration.

Figure C.3 SJE in Panda arm joint 3 without dithering.

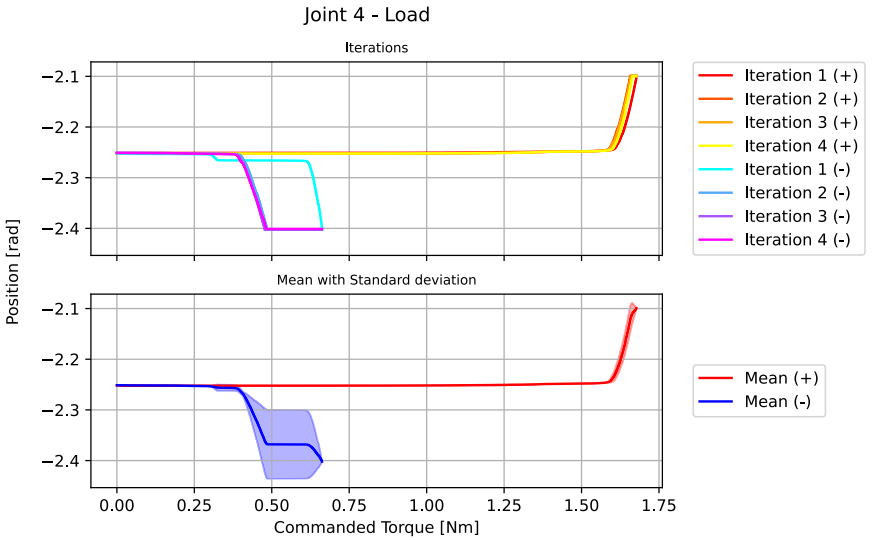

(a) Load configuration.

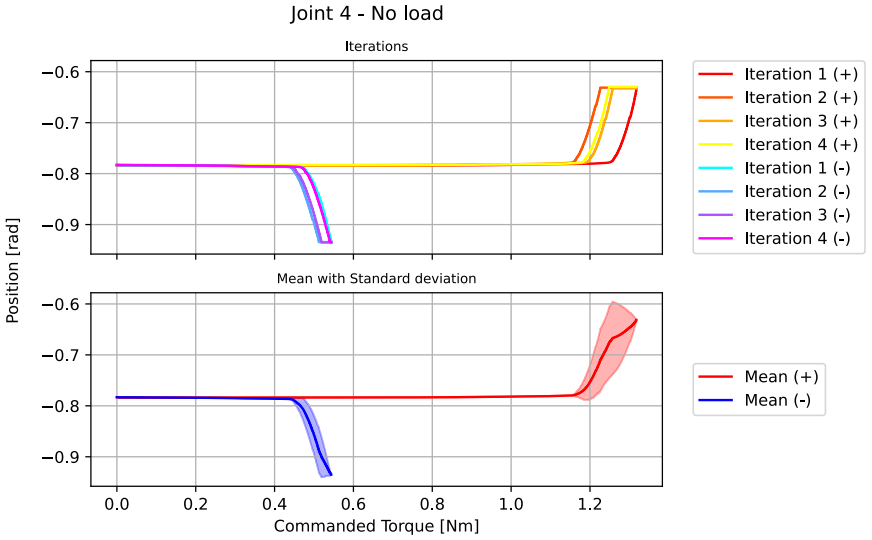

(b) No Load configuration.

Figure C.4 SJE in Panda arm joint 4 without dithering.

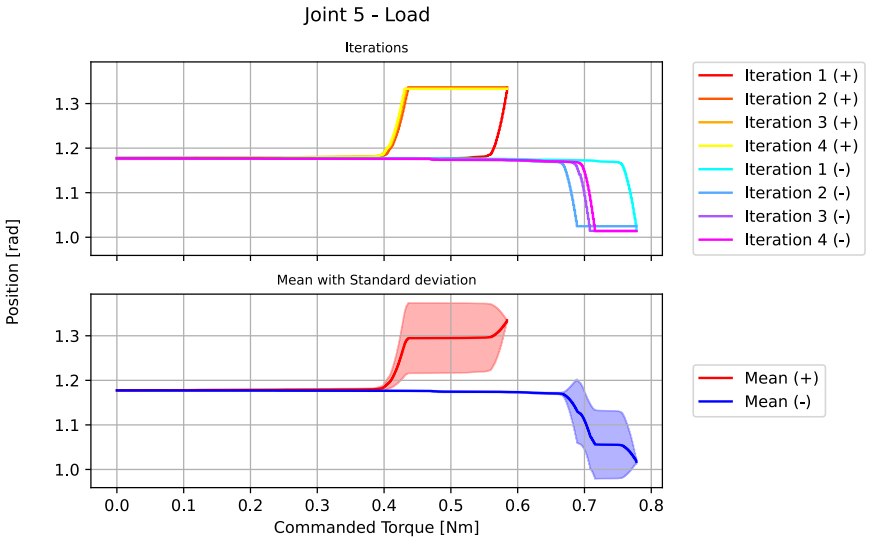

(a) Load configuration.

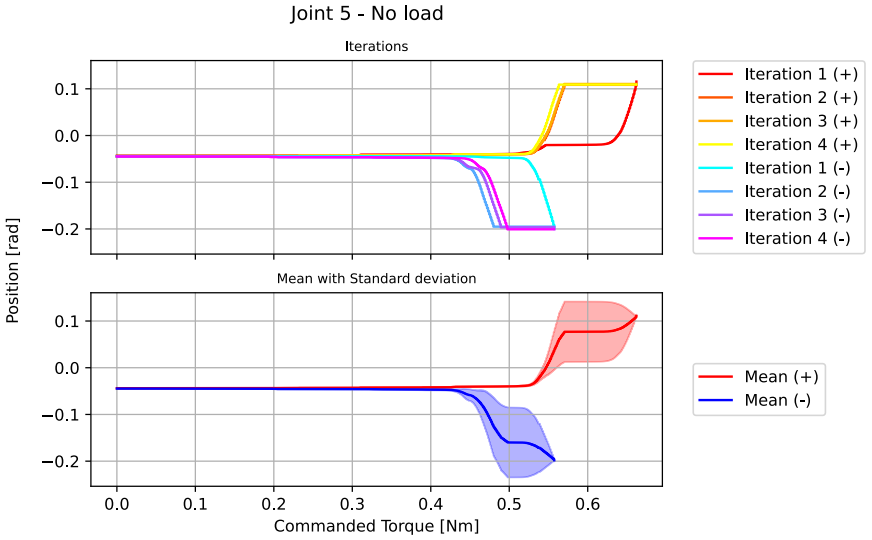

(b) No Load configuration.

Figure C.5 SJE in Panda arm joint 5 without dithering.

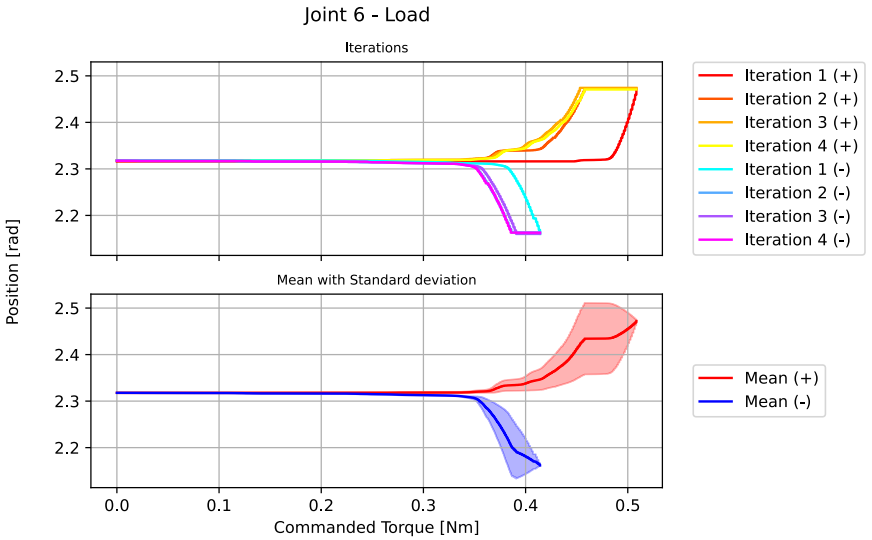

(a) Load configuration.

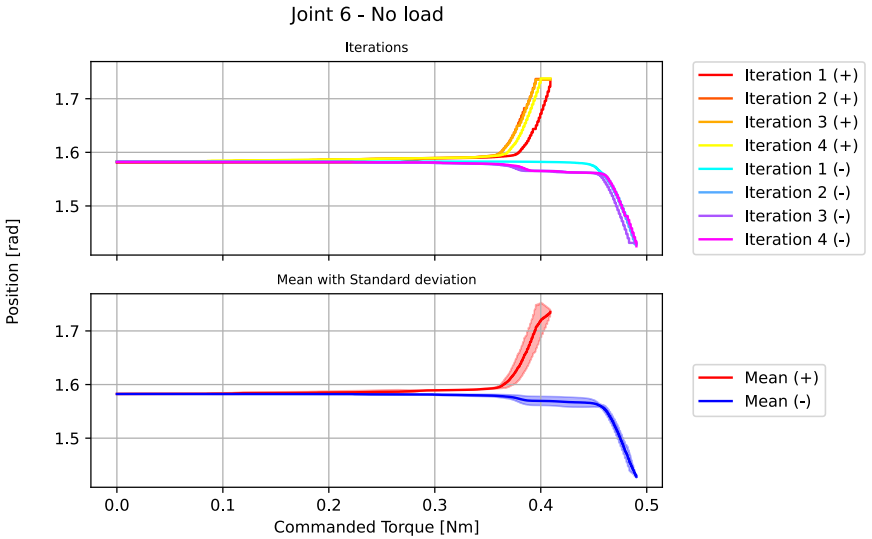

(b) No Load configuration.

Figure C.6 SJE in Panda arm joint 6 without dithering.

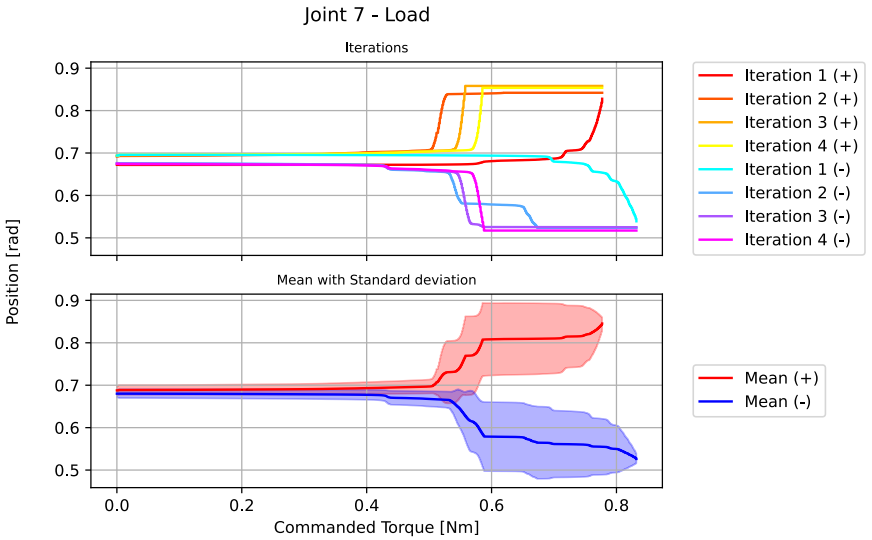

(a) Load configuration.

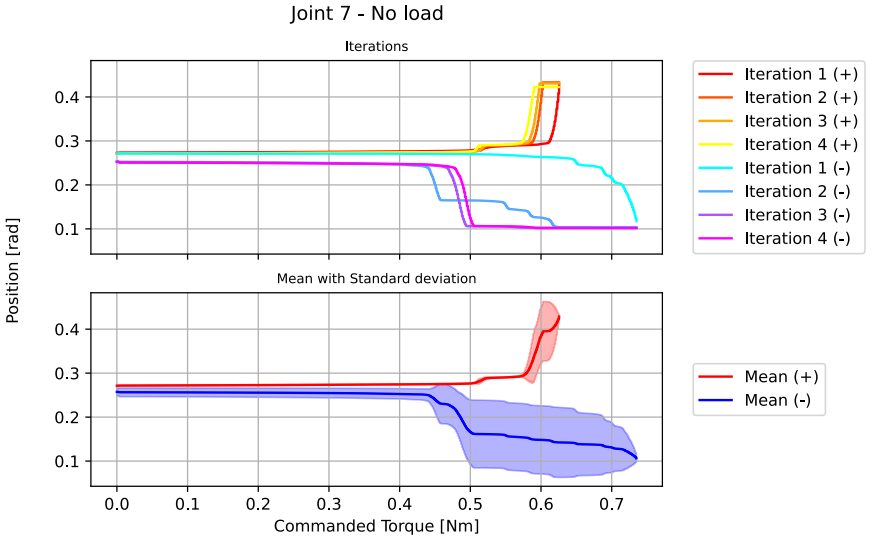

(b) No Load configuration.

Figure C.7 SJE in Panda arm joint 7 without dithering.

D

Appendix — Final Dithered Single Joint Experiment Plots for Panda Arm

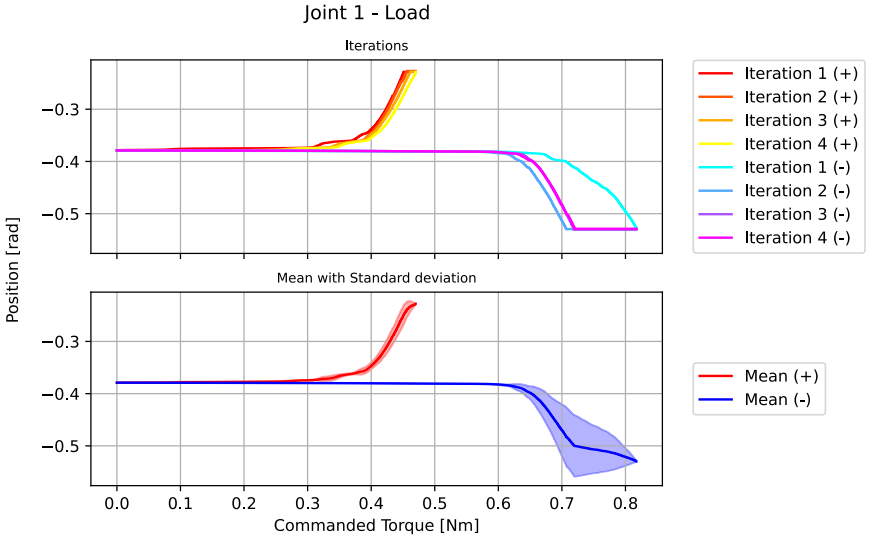

(a) Load configuration.

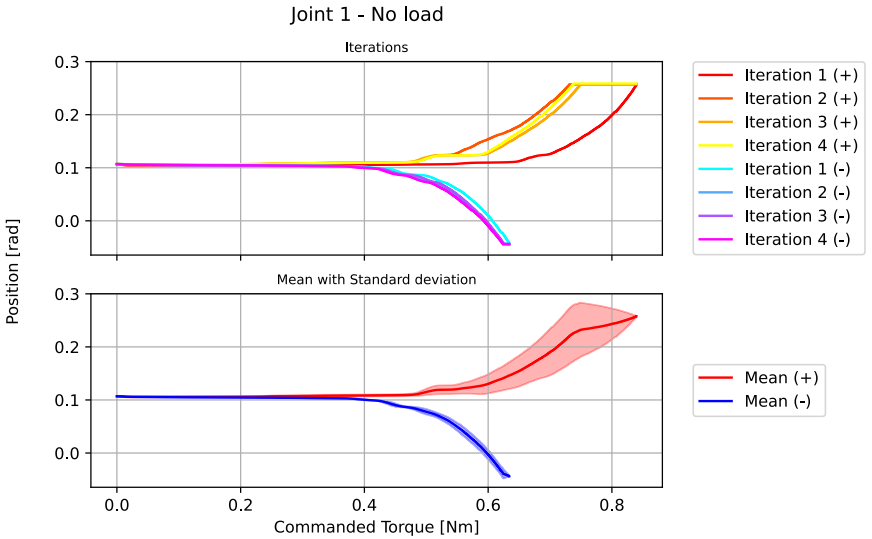

(b) No Load configuration.

Figure D.1 SJE in Panda arm joint 1 with *final* values dithering applied.

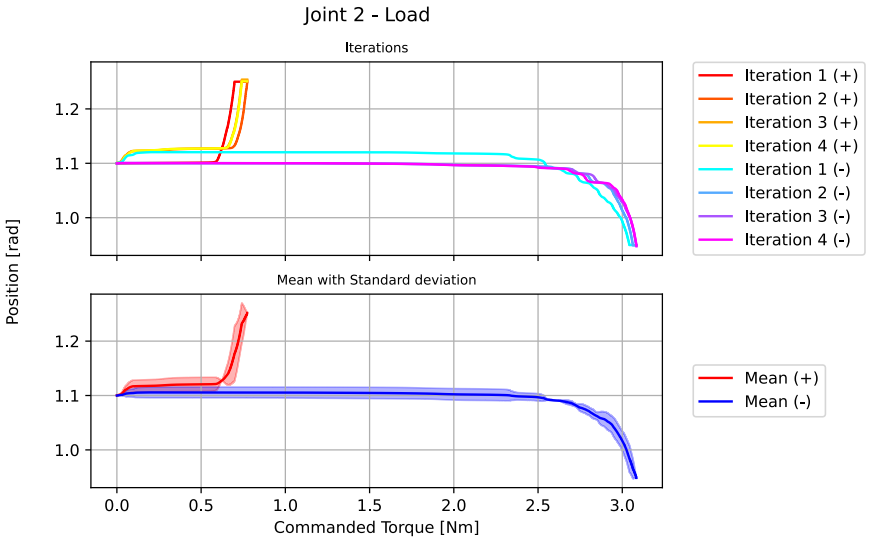

(a) Load configuration.

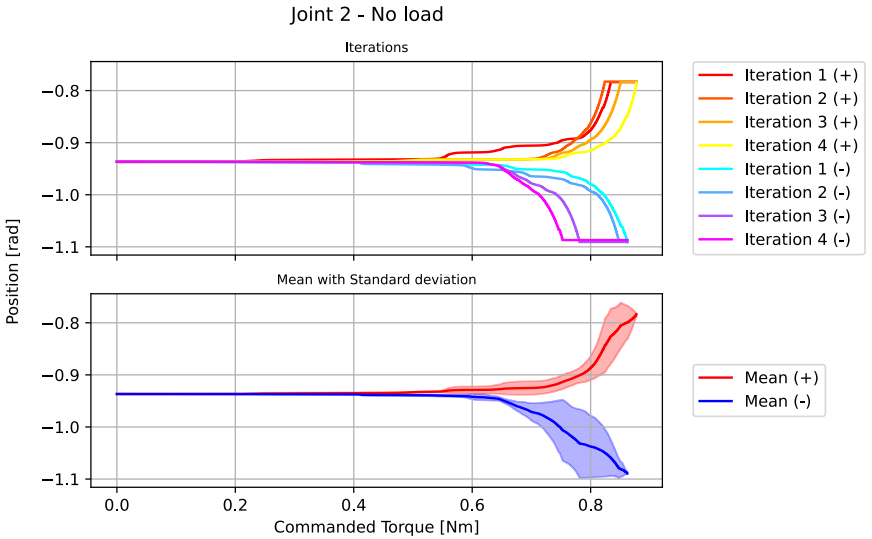

(b) No Load configuration.

Figure D.2 SJE in Panda arm joint 2 with *final* values dithering applied.

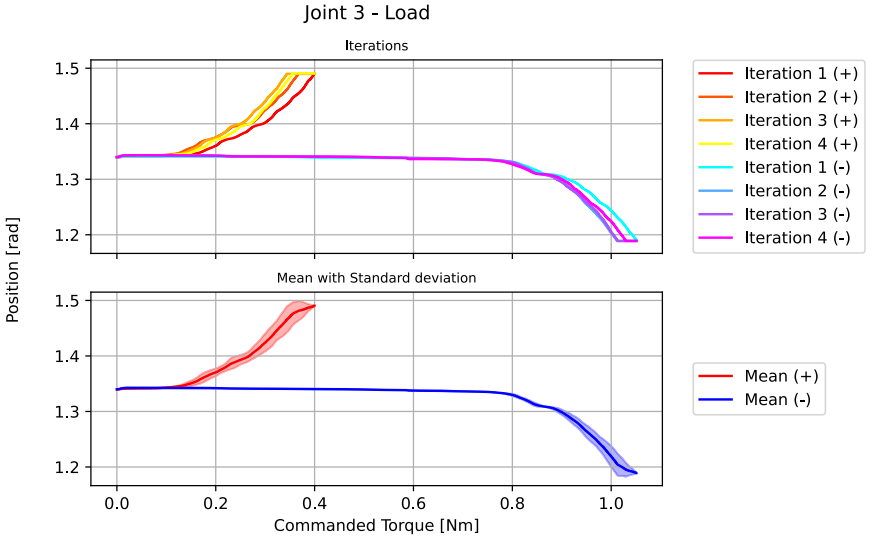

(a) Load configuration.

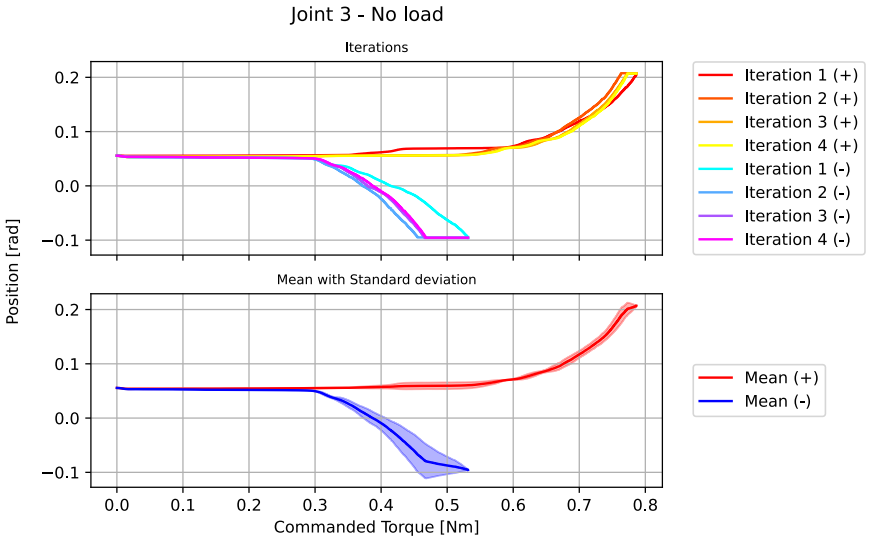

(b) No Load configuration.

Figure D.3 SJE in Panda arm joint 3 with *final* values dithering applied.

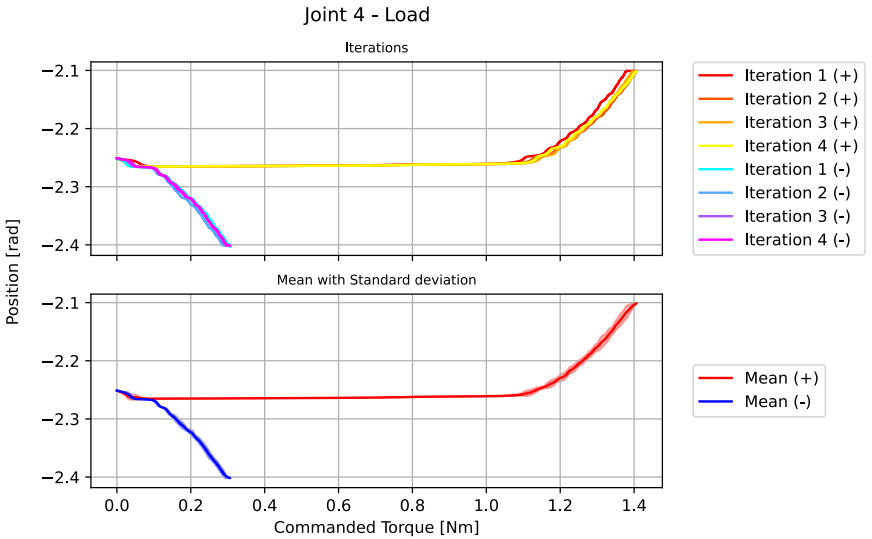

(a) Load configuration.

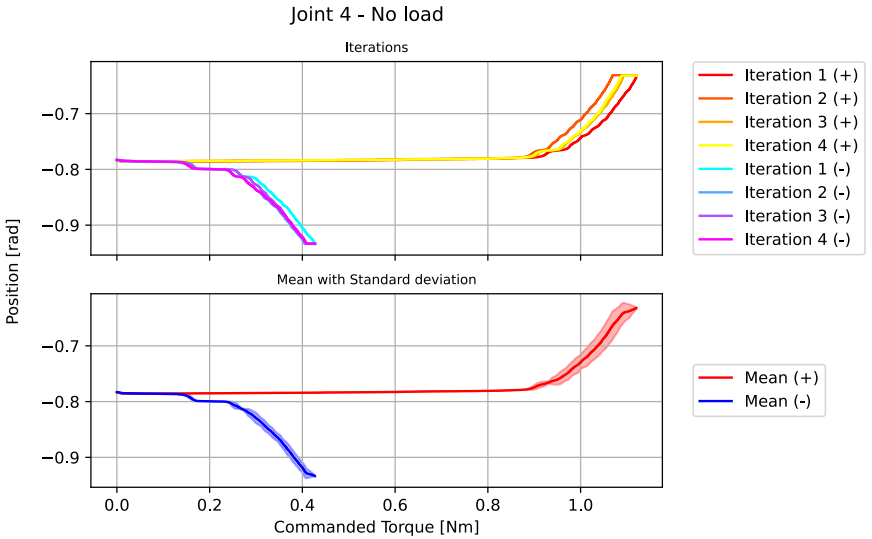

(b) No Load configuration.

Figure D.4 SJE in Panda arm joint 4 with *final* values dithering applied.

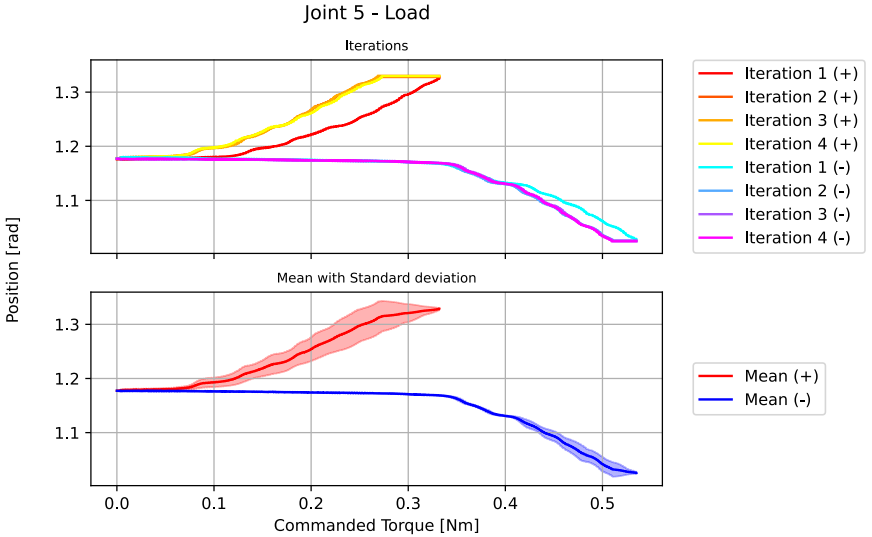

(a) Load configuration.

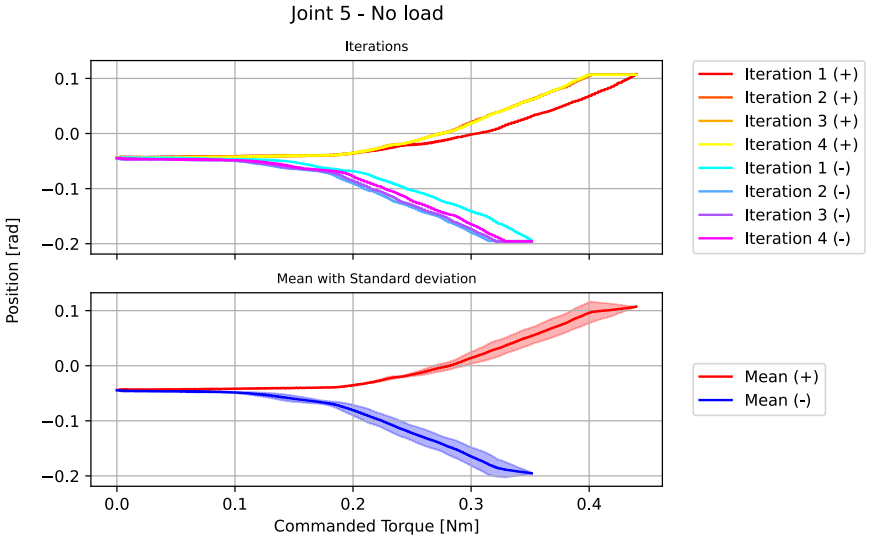

(b) No Load configuration.

Figure D.5 SJE in Panda arm joint 5 with *final* values dithering applied.

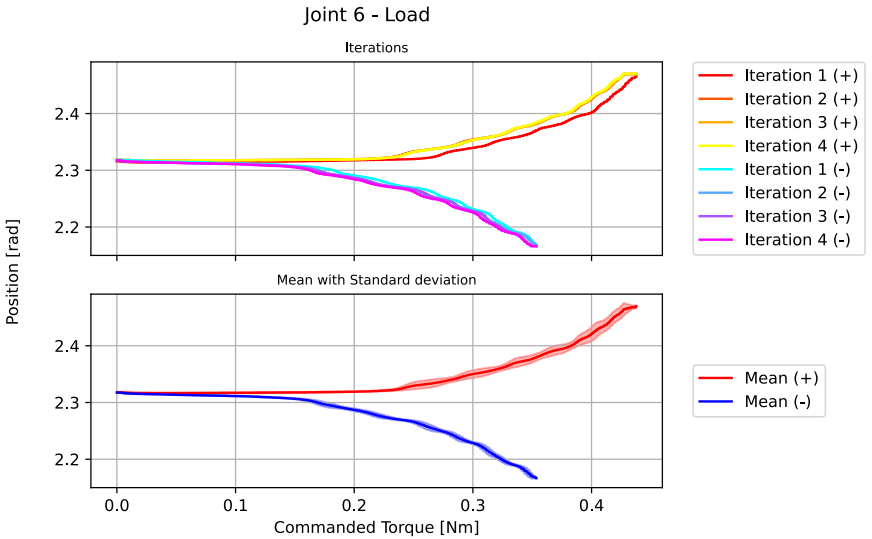

(a) Load configuration.

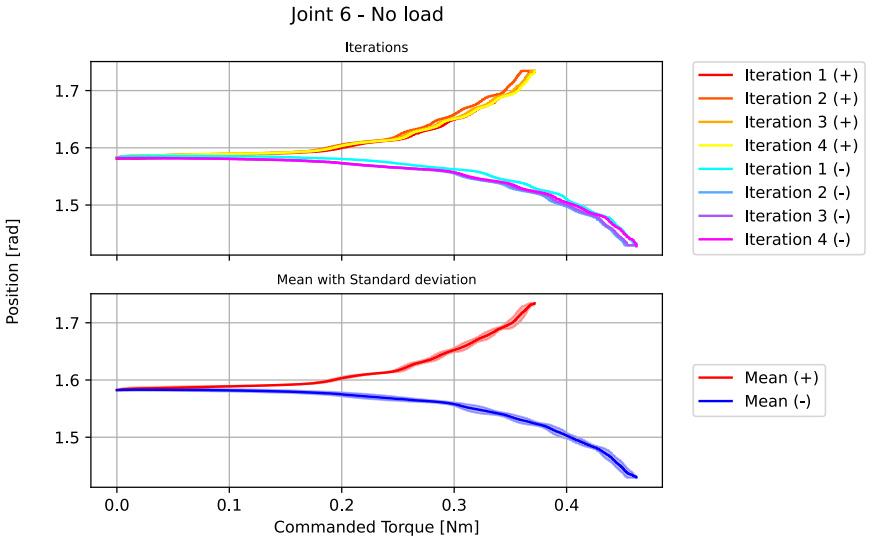

(b) No Load configuration.

Figure D.6 SJE in Panda arm joint 6 with *final* values dithering applied.

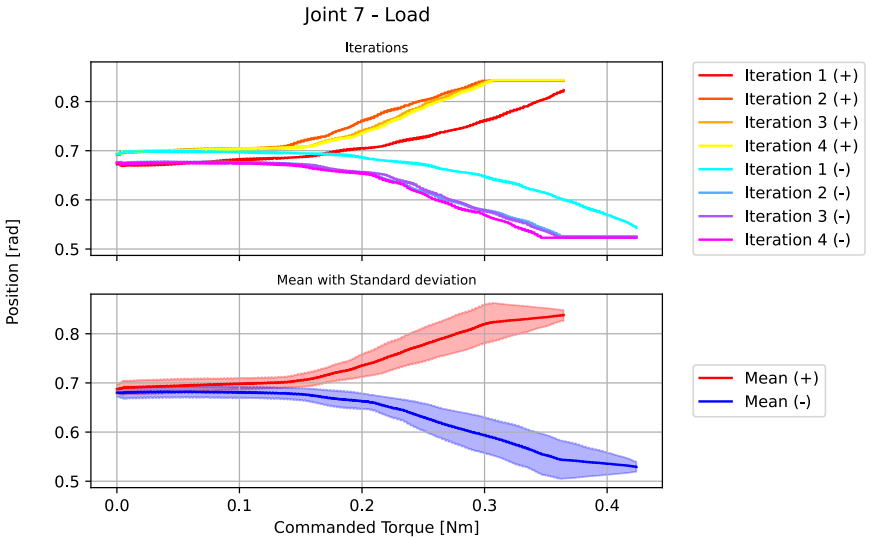

(a) Load configuration.

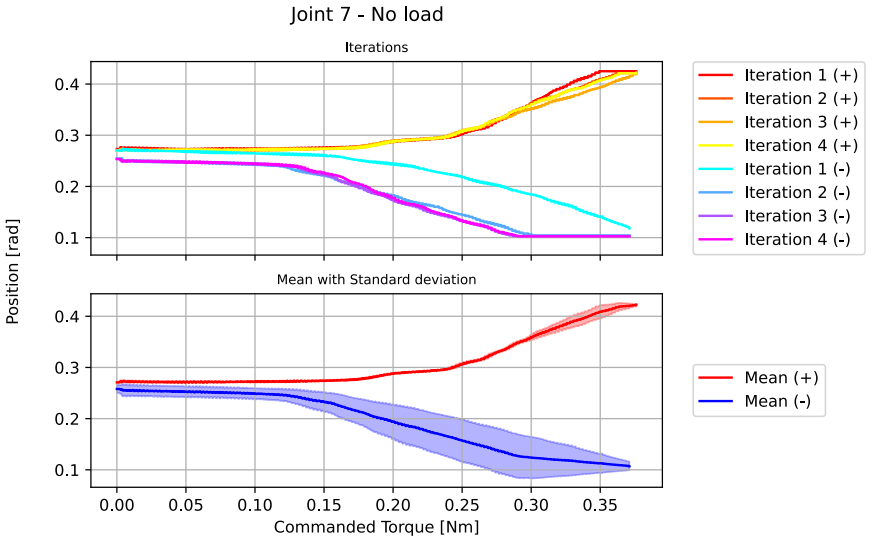

(b) No Load configuration.

Figure D.7 SJE in Panda arm joint 7 with *final* values dithering applied.

E

Appendix — 3D Plots for Generated Trajectory Experiment

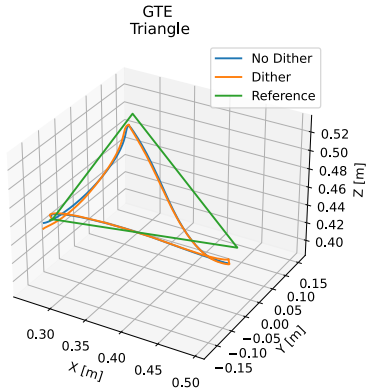

(a) Triangle with 200/20/0 stiffness.

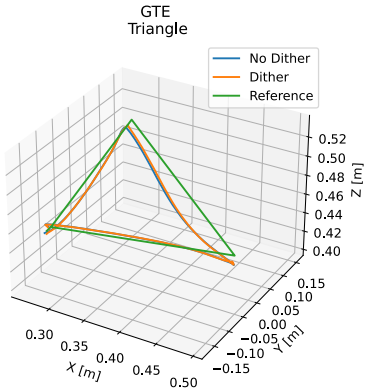

(b) Triangle with 400/40/0 stiffness.

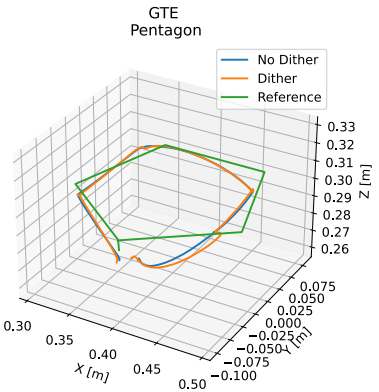

(c) Pentagon with 200/20/0 stiffness.

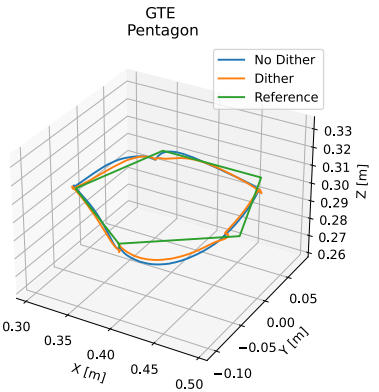

(d) Pentagon with 400/40/0 stiffness.

Figure E.1 Triangle and pentagon 3D trajectory results from the GTE.

F

Appendix — Orientation Error Trajectory Plots for Panda Arm

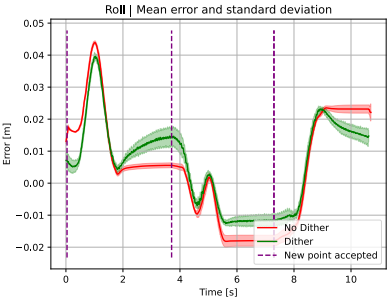

(a) Roll, 200/20/0 stiffness.

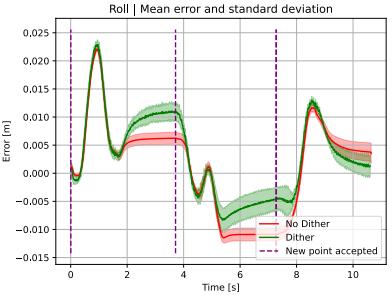

(b) Roll, 400/40/0 stiffness.

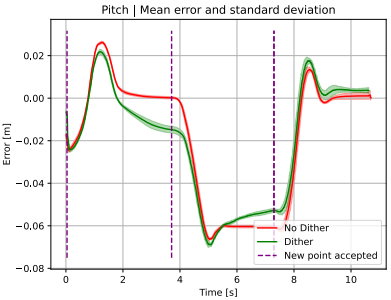

(c) Pitch, 200/20/0.

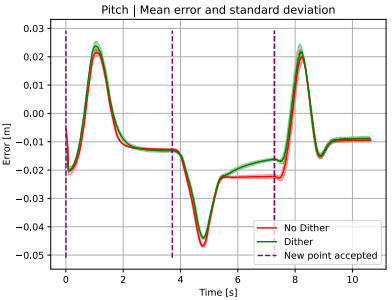

(d) Pitch, 400/40/0.

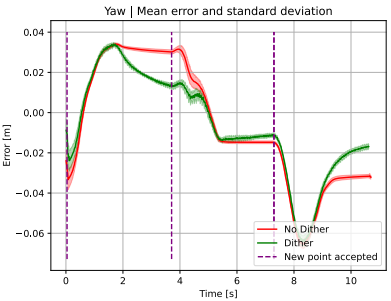

(e) Yaw, 200/20/0.

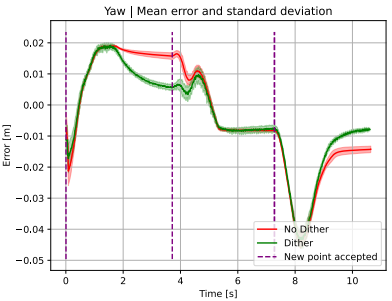

(f) Yaw, 400/40/0.

Figure F.1 Mean error and standard deviation orientation results for the triangle trajectory from the GTE.

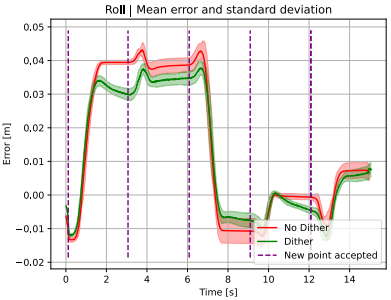

(a) Roll, 200/20/0 stiffness.

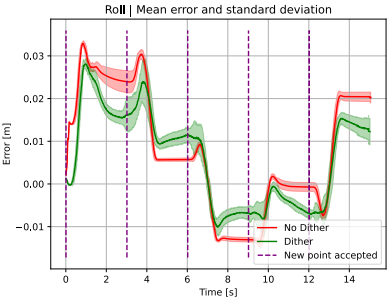

(b) Roll, 400/40/0 stiffness.

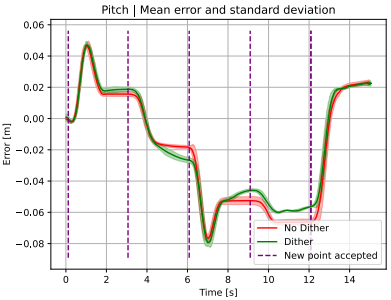

(c) Pitch, 200/20/0.

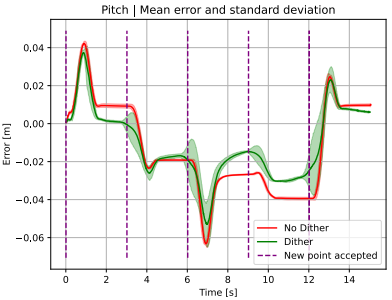

(d) Pitch, 400/40/0.

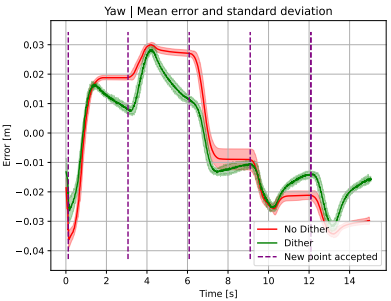

(e) Yaw, 200/20/0.

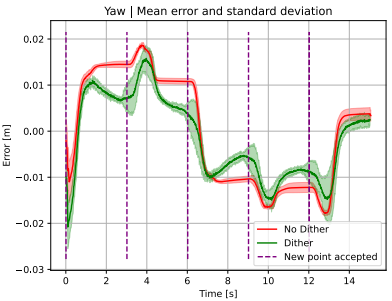

(f) Yaw, 400/40/0.

Figure F.2 Mean error and standard deviation orientation results for the pentagon trajectory from the GTE.

Bibliography

6 Major Causes Of Static Friction (2023). URL: https://afrilcate.com/causes-of-static-friction/ (visited on 2023-04-15).

6 Types of Industrial Robotic Arms (2023). https://www.universal-robots.com/in/blog/types-of-robotic-arms/. (Visited on 2023-03-04).

Chatzilygeroudis, K., M. Mayr, B. Fichera, and A. Billard (2019). *iiwa_ros: A ROS Stack for KUKA's IIWA robots using the Fast Research Interface*. URL: http://github.com/epfl-lasa/iiwa_ros (visited on 2023-06-07).

Chitta, S., E. Marder-Eppstein, W. Meeussen, V. Pradeep, A. Rodríguez Tsouroukdissian, J. Bohren, D. Coleman, B. Magyar, G. Raiola, M. Lüdtke, and E. Fernández Perdomo (2017). "ros_control: A generic and simple control framework for ROS". *The Journal of Open Source Software*. DOI: 10.21105/joss.00456.

Chouman, O. (2021). *Compliance of a Robot Arm using Torque-Based Cartesian Impedance Control*. Master's Thesis. TFRT-6147. Lund University.

Coleman, D., I. A. Sucan, S. Chitta, and N. Correll (2014). "Reducing the barrier to entry of complex robotic software: a moveit! case study". *CoRR* **abs/1404.3785**. arXiv: 1404.3785. URL: http://arxiv.org/abs/1404.3785 (visited on 2023-06-07).

Corke, P. (2017). *Robotics, Vision and Control: Fundamental Algorithms In MATLAB®*. Second. Vol. 118. Springer Tracts in Advanced Robotics. Springer International Publishing. DOI: 10.1007/978-3-319-54413-7.

Craig, J. J. (1989). *Introduction to Robotics: Mechanics and Control*. 2nd. Addison-Wesley Longman Publishing Co., Inc., USA. ISBN: 0201095289. DOI: 10.5555/534661.

Dong, X. X., G. Li, G. F. Liu, and J. Zhao (2012). "Cartesian Impedance Control for Space Robotic Arm Based on End Force/Torque Sensor". *Applied Mechanics and Materials* **268-270**, pp. 1531–1537. ISSN: 1662-7482. DOI: 10.4028/www.scientific.net/AMM.268-270.1531.

Franka Emika Github (2023). URL: https://frankaemika.github.io/docs/overview.html (visited on 2023-04-09).

Franka Emika Robot's Datasheet (2023). URL: https://www.generationrobots.com/media/panda-franka-emika-datasheet.pdf (visited on 2023-04-04).

Franka Emika Robot's Instruction Handbook (2023). URL: https://www.generationrobots.com/media/franka-emika-robot-handbook.pdf (visited on 2023-04-04).

Hogan, N. (1984). "Impedance control: an approach to manipulation". In: *1984 American Control Conference*, pp. 304–313. DOI: 10.23919/ACC.1984.4788393.

Holmesson, J. (2021). *Accurate Simulation of a Collaborative Robot Arm with Cartesian Impedance Control*. Master's Thesis. TFRT-6142. Lund University.

Koenig, N. and A. Howard (2004). "Design and use paradigms for gazebo, an open-source multi-robot simulator". In: *Proceedings of the 2004 IEEE/RSJ International Conference on Intelligent Robots and Systems (IROS)*. Vol. 3, pp. 2149–2154. DOI: 10.1109/IROS.2004.1389566.

LBR iiwa | KUKA AG (2023). URL: https://www.kuka.com/en-de/products/robot-systems/industrial-robots/lbr-iiwa (visited on 2023-04-04).

LBR iiwa KUKA Datasheet (2023). URL: https://www.kuka.com/event/media?itemId=BC8B6EAE73F9447F936084BE87DB1063 (visited on 2023-04-08).

Lee, C. (1982). "Robot arm kinematics, dynamics, and control". *Computer* **15**:12, pp. 62–80. ISSN: 1558-0814. DOI: 10.1109/MC.1982.1653917.

Mayr, M. and J. M. Salt-Ducaju (2022). *A C++ Implementation of a Cartesian Impedance Controller for Robotic Manipulators*. DOI: 10.48550/ARXIV.2212.11215. URL: https://arxiv.org/abs/2212.11215.

Miller, S. J. (2006). "The method of least squares". *Mathematics Department, Brown University* **8**, pp. 1–7.

Ott, C. (2008). *Cartesian Impedance Control of Redundant and Flexible-Joint Robots*. Springer Tracts in Advanced Robotics. Springer Berlin Heidelberg. ISBN: 9783540692553. DOI: 10.1007/978-3-540-69255-3.

Quigley, M., B. Gerkey, K. Conley, J. Faust, T. Foote, J. Leibs, E. Berger, R. Wheeler, and A. Ng (2009). "ROS: an open-source Robot Operating System". In: *Proc. of the IEEE Intl. Conf. on Robotics and Automation (ICRA) Workshop on Open Source Robotics*. Kobe, Japan.

rqt_reconfigure (2023). URL: http://wiki.ros.org/rqt_reconfigure (visited on 2023-06-07).

Rviz Visualization Tool (2023). URL: http://wiki.ros.org/rviz (visited on 2023-06-07).

Salt Ducaju, J., B. Olofsson, A. Robertsson, and R. Johansson (2021). "Joint stiction avoidance with null-space motion in real-time model predictive control for redundant collaborative robots". English. In: *2021 30th IEEE International Conference on Robot and Human Interactive Communication, RO-MAN 2021*. IEEE International Conference on Robot and Human Interactive Communication, RO-MAN. Conference date: 08-08-2021 Through 12-08-2021. IEEE - Institute of Electrical and Electronics Engineers Inc., United States, pp. 307–314. DOI: 10.1109/RO-MAN50785.2021.9515514.

Siciliano, B. and O. Khatib (2007). *Springer Handbook of Robotics*. Springer-Verlag, Berlin, Heidelberg. ISBN: 354023957X.

Siciliano, B., L. Sciavicco, L. Villani, and G. Oriolo (2008). *Robotics: Modelling, Planning and Control*. 1st. Springer Publishing Company, Incorporated, London. ISBN: 1846286417.

Spong, M. W. and M. Vidyasagar (1989). *Robot Dynamics and Control*. John Wiley and Sons, New York.

Stolt, A. (2015). *On robotic assembly using contact force control and estimation*. PhD Thesis. TFRT-1109. Lund University.

Stolt, A., A. Robertsson, and R. Johansson (2015). "Robotic force estimation using dithering to decrease the low velocity friction uncertainties". English. In: *2015 IEEE International Conference on Robotics and Automation (ICRA)*. Conference date: 26-05-2015 Through 30-05-2015. IEEE - Institute of Electrical and Electronics Engineers Inc., United States, pp. 3896–3902. ISBN: 978-1-4799-6924-1. DOI: 10.1109/ICRA.2015.7139742.

TriboNet (2023). *Stribeck Curve - About Tribology*. en-US. URL: https://www.tribonet.org/wiki/stribeck-curve/ (visited on 2023-04-12).